Stratospheric Aerosols, Polar Stratospheric Clouds, and Polar Ozone Depletion After the Mount Calbuco Eruption in 2015

Yunqian Zhu, Owen Brian Toon, Douglas Kinnison, V. Lynn Harvey, Michael Mills, Charles G Bardeen, Michael Pitts, Nelson Bègue, Jean-Baptiste Renard, Gwenaël Berthet, et al.

Journal of Geophysical Research: Atmospheres

RESEARCH ARTICLE
10.1029/2018JD028974

Stratospheric Aerosols, Polar Stratospheric Clouds, and Polar Ozone Depletion After the Mount Calbuco Eruption in 2015

Yunqian Zhu[1], Owen Brian Toon[1,2], Douglas Kinnison[3], V. Lynn Harvey[1], Michael J. Mills[3], Charles G. Bardeen[3], Michael Pitts[4], Nelson Bègue[5], Jean-Baptiste Renard[6], Gwenaël Berthet[6], and Fabrice Jégou[6]

[1]Laboratory for Atmospheric and Space Physics, University of Colorado Boulder, Boulder, CO, USA, [2]Department of Atmospheric and Oceanic Sciences, University of Colorado Boulder, Boulder, CO, USA, [3]Atmospheric Chemistry Observations and Modeling Laboratory, National Center for Atmospheric Research, Boulder, CO, USA, [4]Langley Research Center, Hampton, VA, USA, [5]Laboratoire de l'Atmosphère et des Cyclones, UMR 8105 CNRS, Université de la Réunion, Saint-Denis, France, [6]Laboratoire de Physique et Chimie de l'Environnement et de l'Espace, Université d'Orléans, Orléans, France

Abstract We investigate the impact of the 2015 Mount Calbuco eruption and previous eruptions on stratospheric aerosols, polar stratospheric clouds, and ozone depletion using the Community Earth System Model coupled with the Community Aerosol and Radiation Model for Atmospheres compared with several satellite and balloon observations. The modeled volcanic sulfate aerosol size distribution agrees with the Light Optical Aerosol Counter observation at the Reunion Island site (21°S, 55°E) on 19 August at 20 km within estimated 0.1- to 1-μm radius error bars. Both the observed and simulated backscatter and extinction show that volcanic sulfate aerosol from the Mount Calbuco eruption was transported from midlatitude toward the Antarctic and slowly descended during transport. They also indicate that the SO_2 emission into the stratosphere from Mount Calbuco is 0.2–0.4 Tg. The modeled number density indicates that the volcanic sulfate aerosol from the Mount Calbuco eruption penetrated into the Antarctic polar vortex in May and thereafter and reduced the polar stratospheric clouds effective radius. In the simulations, the Antarctic stratosphere denitrified too early and by too much compared with Microwave Limb Sounder observations. Heterogeneous nucleation of nitric acid trihydrate or sophisticated gravity wave representations may be required to simulate nitric acid trihydrate particles with smaller falling velocity. The volcanic sulfate aerosol increases the ozone depletion in September especially around 100 hPa and 70°S, relative to a case without any volcanic eruptions. The simulated surface area density, earlier ozone loss, and larger area of the ozone hole are consistent with the presence of volcanic sulfate layers observed at 16 km as well as previous studies.

Key Points:
- The simulated sulfate aerosol are generally consistent with balloon and satellite data, but simulated PSCs over-denitrify the Antarctic
- The simulated volcanic sulfate aerosol from the Mount Calbuco eruption penetrated into the Antarctic vortex in May 2015 and thereafter
- Volcanic sulfate aerosol from Mount Calbuco and previous eruptions causes the ozone hole to develop earlier in the year and has a larger area

Correspondence to:
Y. Zhu,
yunqian.zhu@colorado.edu

Citation:
Zhu, Y., Toon, O. B., Kinnison, D., Harvey, V. L., Mills, M. J., Bardeen, C. G., et al. (2018). Stratospheric aerosols, polar stratospheric clouds, and polar ozone depletion after the Mount Calbuco eruption in 2015. *Journal of Geophysical Research: Atmospheres*, *123*. https://doi.org/10.1029/2018JD028974

Received 24 MAY 2018
Accepted 23 OCT 2018
Accepted article online 27 OCT 2018

1. Introduction

Small volcanic eruptions can enhance stratospheric aerosols enough to impact stratospheric chemistry and the atmospheric radiation budget (Santer et al., 2014). Increased stratospheric aerosols since 2002, likely due to small volcanic eruptions (Neely et al., 2013; Vernier et al., 2011), have been observed by various in situ and remote platforms (Hofmann et al., 2009; Ridley et al., 2014; Trickl et al., 2013; Vernier et al., 2011). This change in aerosols may have contributed to a slowing of the rate of increase of surface temperature, the so-called global warming *hiatus* (Solomon et al., 2011). Recent studies have shown that quite small climate changes are observable following small eruptions (Santer et al., 2014), and minor volcanic eruptions are likely to affect stratospheric circulation in terms of age of air (Diallo et al., 2017). In addition, stratospheric chemistry changes have been observed due to heterogeneous reactions on volcanic particles, changes in stratosphere temperature, and changes in ozone photolysis reactions (Crutzen, 1976; Solomon et al., 1996; Tie & Brasseur, 1995; Tie et al., 1996). Ozonesonde and satellite observations show enhanced midlatitude and Antarctic ozone loss following the large volcanic eruptions of Mount Pinatubo in 1991 and El Chichon in 1982 (Hofmann & Oltmans, 1993; Solomon et al., 2005). It has recently been suggested that small volcanic eruptions might also impact stratospheric ozone. Solomon et al. (2016) found that small eruptions in the Southern Hemisphere (SH) have caused the area of the ozone hole to expand significantly in the year following these eruptions, delaying the recovery of the ozone hole.

For this study, we investigate the impact of the Mount Calbuco eruption on the stratospheric sulfate aerosol and on the Antarctic ozone hole of 2015. Mount Calbuco, located in Chile at 41°S and 73°W, erupted several

times in April 2015 and emitted ~0.4 Tg of SO_2 into the atmosphere as high as 21 km (Bègue et al., 2017; Mills et al., 2016; Solomon et al., 2016). Satellite observations (discussed in section 4.2) show the volcanic sulfate aerosol extended past the tip of South America, and remained abundant in October of 2015 when the ozone hole typically forms. Stone et al. (2017) and Ivy et al. (2017) conducted detailed analyses of ozone depletion after the 2015 Mount Calbuco eruption. These studies used the Chemistry Climate Model Initiative (CCMI) version of the Community Earth System Model version 1 (CESM1) Whole Atmosphere Community Climate Model (WACCM). This version of WACCM also used the volcanic aerosol properties based on the work of Mills et al. (2016) and discussed in Solomon et al. (2016). The aerosol size distributions are represented by multiple lognormal functions in their modal aerosol model. In the remaining discussion, we will refer to this version of the model as Solomon et al. (2016). Stone et al. (2017) found the simulated backscatter of the volcanic sulfate aerosol was consistent with the Cloud-Aerosol Lidar and Infrared Pathfinder Satellite Observations(CALIPSO) and found enhanced ozone depletion particularly at 150–100 hPa and 55–68°S. Ivy et al. (2017) found the enhanced ozone depletion was mostly caused by the volcanic aerosol, while the effect of dynamic or thermal feedbacks on ozone was minimal. We apply the same dynamical and chemical model, but with a different aerosol package using a sectional method, the Community Aerosol and Radiation Model for Atmospheres (CARMA), to simulate sulfuric acid aerosol and polar stratospheric clouds (PSCs) interactively (detailed in section 3). *Sectional* means the aerosol size distribution is computed in a number of size bins without any assumptions about its shape. In this paper, we introduce the model and the data we use to explore the following science questions.

1. How do the size distributions of PSCs and sulfuric acid aerosol change due to the injection of SO_2 from the Mount Calbuco eruptions? How does the size distribution affect the aerosol extinction and phase function?
2. How do the simulated optical properties of sulfuric acid aerosol and PSCs compare with observations from the CALIPSO, the Suomi National Polar-orbiting Partnership Ozone Mapping and Profiler Suite Limb Profiler (OMPS LP), and the Optical Spectrograph and InfraRed Imager System (OSIRIS) satellites in the SH? How do the sulfate aerosol evolve with time and enter the Antarctic polar vortex?
3. How does the simulated evolution of gas phase HNO_3 near the South Pole compare with the Microwave Limb Sounder (MLS) observations?
4. Do volcanic sulfuric acid aerosol and perturbed PSCs enhance ozone depletion and expand the area of the ozone hole as found by Solomon et al. (2016)? How do our sectional simulations of surface area density (SAD) compare with simulations using a modal aerosol model by Solomon et al. (2016), Stone et al. (2017), and Ivy et al. (2017)?

2. Observations

2.1. Cloud-Aerosol Lidar and Infrared Pathfinder Satellite Observations

The Cloud-Aerosol Lidar with Orthogonal Polarization instrument aboard the CALIPSO spacecraft is a two-wavelength, polarization sensitive lidar. It provides high-resolution profiles of backscatter coefficients at 532 and 1,064 nm, and two orthogonal (parallel and perpendicular) polarization components at 532 nm (Winker et al., 2007). Vertical resolution can be as high as 60–180 m for the lower stratosphere where volcanism perturbs the aerosols and the PSCs often occur. We use the level 1B nighttime aerosol data version 4.1 and level 2 PSC mask data version 1 products to explore the backscatter coefficient, backscattering ratio, and depolarization from sulfate aerosol and PSCs.

2.2. Suomi-National Polar-Orbiting Partnership OMPS LP

The OMPS LP (Flynn et al., 2006) data have been processed to create an aerosol extinction coefficient product based on 675-nm radiance measurements. Loughman et al. (2017) describe the version 1.0 675-nm extinction coefficient that we will compare with the modeled results. The algorithm assumes spherical particles of sulfuric acid with a refractive index of 1.448, and with a bimodal lognormal size distribution with modal radii of 0.09 and 0.32 μm, and mode widths (geometric standard deviations) of 1.4 and 1.6 for fine and coarse mode particles, respectively. The coarse mode fraction (ratio of the coarse mode particle concentration to the total particle concentration) is assumed to be 0.003. These values are based on aircraft measurements from August 1991 (Pueschel et al., 1994), with the coarse mode fraction adjusted to provide an Ångström exponent of 2.0, in order to match the average value of Ångström exponent determined from the

Table 1
The Precision and Accuracy for MLS HNO_3, O_3 Version 4.2 Data Set (Livesey, 2015) for the Lower Stratosphere

HNO_3			O_3		
Pressure (hPa)	Precision (ppbv)	Accuracy (ppbv)	Pressure (hPa)	Precision (ppmv)	Accuracy (ppmv)
15–4.6 22	±0.6	±0.5	10	0.1	0.3
32	±0.6	±2.4	22	0.1	0.2
147–46	±0.6	±1.5	46	0.06	0.2
215	±0.6	±1.0	68	0.04	0.05
	±0.6	±1.1	100	0.03	0.05 + 5%
			150	0.02	0.02 + 5%
			215	0.02	0.02 + 20%

Note. The O_3 215- to 100-hPa accuracies are the sum of the ppmv and percentage scaling uncertainties quoted. MLS = Microwave Limb Sounder.

Stratospheric Aerosol and Gas Experiment II data taken during 2000–2005. The bimodal distribution is used because it describes the observed stratospheric aerosol better than a unimodal distribution according to SPARC (2006); however, a fixed size distribution limits the ability to represent changes due to eruptions because volcanic sulfate aerosol would not be expected to have the same size distribution as the unperturbed sulfate aerosol.

2.3. Optical Spectrograph and Infrared Imager System

The OSIRIS instrument launched in 2001 on board the Odin satellite (Llewellyn et al., 2004) is a limb scatter instrument that has been used to retrieve aerosol extinction at 750 nm (Bourassa et al., 2012). This study utilizes the version 5.07 aerosol extinction product at 750 nm, which showed agreement within approximately 10% throughout the 15- to 25-km altitude range with Stratospheric Aerosol and Gas Experiment III 755-nm extinction data from 2002 to 2005 (Bourassa et al., 2012). In the OSIRIS retrieval, the stratospheric aerosols are assumed to be composed of 75% H_2SO_4 and 25% H_2O and to have a lognormal particle size distribution with a mode width of 1.6 and mode radius of 0.08 μm based on the optical particle counter (OPC) data (Deshler et al., 2003) but excluding coarse mode particles. This size distribution corresponds to an Ångström exponent of 2.3. However, after the OSIRIS version 5.07 aerosol extinction product was released Kovilakam and Deshler (2015) present a corrected version of the balloon-borne OPC data. OPC calculated extinction increased by up to 30% for volcanic measurements and up to 50% for nonvolcanic cases using this correction. Therefore, using the noncorrected OPC data may introduce errors for OSIRIS extinction retrieval. Additionally, a volcanic cloud would not be expected to have the same size distribution as the unperturbed aerosol.

2.4. Microwave Limb Sounder

The MLS instrument on board National Aeronautics and Space Administration's Earth Observing System Aura satellite (Schoeberl, 2007) provides gas phase HNO_3 and O_3 profiles for this study. We use the version 4.2 data set described by (Livesey, 2015). Table 1 shows the precision and accuracy of the measurement for chemicals in the lower stratosphere.

2.5. Light Optical Aerosol Counter

After the Mount Calbuco eruption, Light Optical Aerosol Counter (LOAC) systems (Bègue et al., 2017; Renard et al., 2016a, 2016b) were launched with latex weather balloons at the Reunion Island site (21°S, 55°E) on 19 May and 19 August 2015. Through the measurements of the light scattered by particles at two specific angles (Lurton et al., 2014), the LOAC provides aerosol concentrations for 19 size classes ranging from 0.2 to 50 μm in diameter with a vertical profile from near the surface to over 30 km. The uncertainties in number concentrations of particles smaller than 1 μm are about 30%, but the uncertainties can be as high as 60% for particle sizes over 1 μm due to the low particle concentrations.

3. Model Description

For this study, we apply a microphysical sulfate and PSC model coupled with the SD version of the WACCM 4.0 (Garcia et al., 2007; Marsh et al., 2013). SD means the model is nudged with the Modern Era Retrospective

Analysis for Research and Applications (Kunz et al., 2011; Lamarque et al., 2012; Rienecker et al., 2011) for temperature, zonal and meridional winds, and surface fields including sensible heat, water vapor flux, and the shear stresses. The volcanic sulfate aerosol is not radiatively active in the model. The model uses a 1.9° latitude × 2.5° longitude horizontal resolution and 88 vertical levels from the surface to about 140 km, with about 1-km vertical resolution in the stratosphere.

The microphysics model is based on the CARMA, developed by Bardeen et al. (2008), Mills et al. (2008), Bardeen et al. (2010), English et al. (2011), Zhu et al. (2015), and Zhu, Toon, Lambert, et al., 2017. The model contains microphysical treatments of sulfuric acid aerosol and three types of PSCs: supercooled ternary solution (STS), nitric acid trihydrate (NAT), and ice. The PSC microphysical processes are described in Zhu et al. (2015) and Zhu, Toon, Lambert, et al. (2017). The main microphysical processes include the growth/evaporation/sedimentation of each particle type; homogenous nucleation from STS to NAT based on the surface nucleation scheme by Tabazadeh et al. (2002) with a modified nucleation free-energy term (Zhu et al., 2015); homogeneous nucleation from STS to ice (Koop et al., 2000); and heterogeneous nucleation from NAT to ice and ice to NAT (Pruppacher & Klett, 1997; Toon et al., 1989). The model has been developed and tested for ambient stratospheric sulfate aerosol and volcanic sulfate aerosol (English et al., 2011, 2013) using free-running WACCM, as well as for PSCs during the Arctic winter of 2010–2011 (Zhu et al., 2015) and the Antarctic winter of 2010 (Zhu, Toon, Lambert, et al., 2017; Zhu, Toon, Pitts, et al., 2017) using SD-WACCM. In this study, the simulated radii of sulfate aerosol and PSCs range from 0.000343 to ~ 80 μm. The number density we discuss in this paper includes all the simulated particles within this range, except Figure 1, in which we show the integral number density from 0.001 to 10 μm to match the plot axis range. The model only considers the possibility of water, sulfuric acid, and nitric acid within the particles. The mixture of sulfate and nonsulfate materials (e.g., volcanic ash, micrometeorites, and organics) and the heterogeneous nucleation of sulfate on nonsulfate materials is not considered. They may change the size distributions and refractive index of stratospheric aerosols that can affect the extinction retrieval.

The model chemistry uses the middle atmosphere Model for Ozone and Related chemical Tracers with sulfur chemistry including reactions involving carbonyl sulfide (OCS), SO, SO_2, S, HSO_3, SO_3, and H_2SO_4 (Campbell et al., 2014; Marsh et al., 2013; Mills et al., 2005). It also treats 18 heterogeneous chemical reactions on sulfate aerosol and PSCs (Kinnison et al., 2007; with updates discussed in Solomon et al., 2015). One difference between our model and the one used by Solomon et al. (2016) is that the stratospheric heterogeneous chemistry is calculated from 300 hPa and above in their model but from the tropopause and above in our model. The tropopause is about 350 hPa near the South Pole and 250 hPa in midlatitude SH. Therefore, when we compare the results between these two models we show our results above the tropopause or 300 hPa, whichever pressure value is lower.

3.1. Volcanic Emissions in the Model

For this study, the only volcanic emissions we consider are SO_2 injections. We ignore volcanic emissions of ash and of other gases, such as H_2O, H_2S, CO_2, or HCl. Our model uses the same database of volcanic sulfur dioxide (SO_2) emissions and plume altitudes based on observations along with nonvolcanic sulfur sources of OCS and SO_2 as the model of Mills et al. (2016), which was used to calculate the volcanic aerosol properties used in Solomon et al. (2016), though we do not include dimethyl sulfide in our chemistry. To initialize the perturbed background sulfate, the model is run for ~ 4 years from 2011 to 2015, including volcanic eruptions of Grímsvötn 2011, Puyehue-Cordón Caulle 2011, Nabro 2011, Nyamuragira 2011, Soputan 2012, Copahue 2012, Paluweh 2013, Sinabung 2014, Kelut 2014, and Sangeang Api 2014, using emissions from Mills et al. (2016).

In order to investigate the effect of the Mount Calbuco eruption and previous eruptions on stratospheric sulfate aerosol, PSCs, and ozone, we conduct several test cases as described in Table 2. In the Base case, we add SO_2 emissions from the Mount Calbuco eruption on 23 April 2015 using the injection profiles from Mills et al. (2016). The eruption occurs in the model over 6 hr between 12:00 UTC and 18:00 UTC, with a constant mass density emission rate ($g{\cdot}cm^{-3}{\cdot}s^{-1}$) and a total injection of 0.4 Tg of SO_2 between 17.4 and 21 km at −41°S, 287°W. We conduct a case (Noemission) without any volcanic eruptions after 2011. We conduct a case (NoCalbuco) with the previous eruptions from 2011 to 2014 but without the Mount Calbuco eruption. The satellite estimated SO_2 injection has uncertainties, and different instruments give

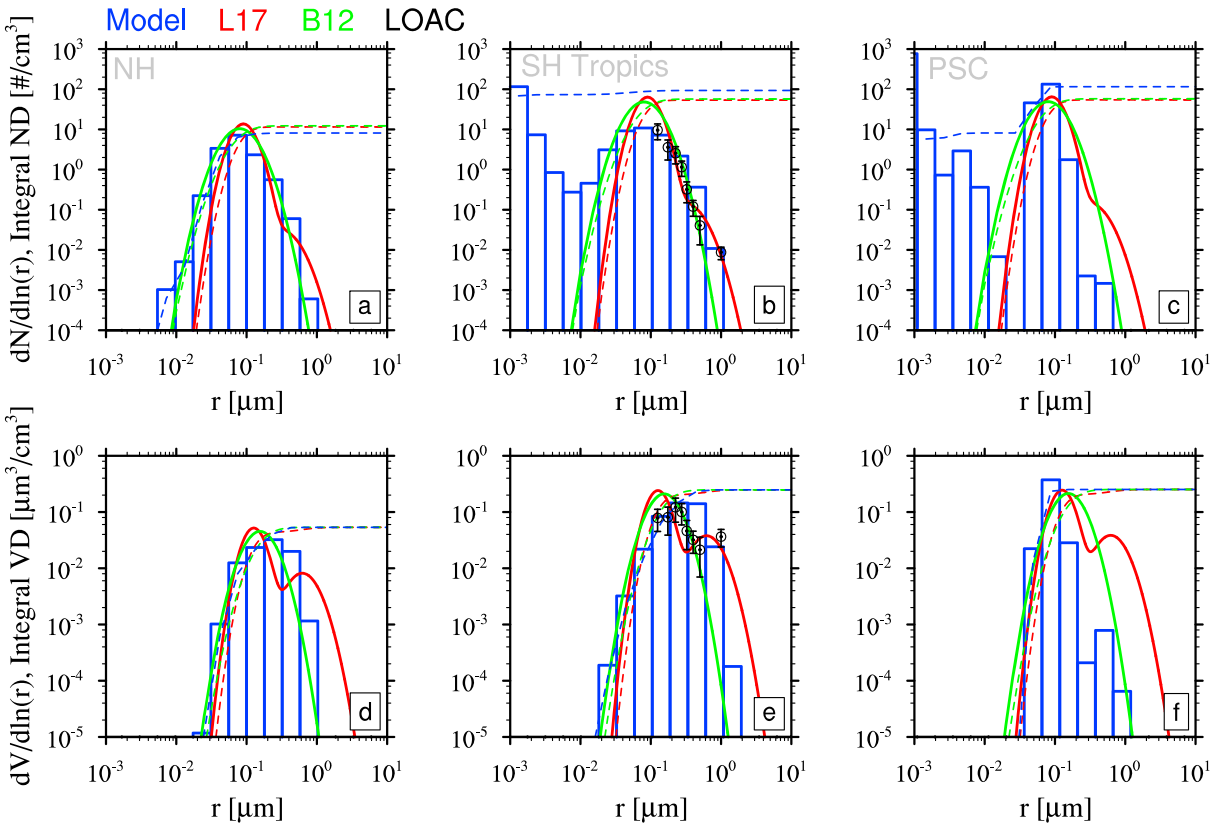

Figure 1. The particle size distribution on 19 August 2015 in the Base case (blue histogram) at 52 hPa, which is ~20 km for NH and SH tropical aerosol and ~18 km for PSCs. The L17 (red solid line) and B12 (green solid line) size distributions assume the same particle volume as the model in each case. The black circles with error bars in the middle panels are LOAC observations at 20 km on 19 August at Reunion Island site. Figures 1a and 1d are sampled in the NH (46°N, 0°E) to represent background sulfate; Figures 1b and 1e are in SH (21°S, 55°E) outside the vortex representing volcanic sulfate aerosol; Figures 1c and 1f are near the Antarctic representing STS (67°S, 245°W). The top rows are number size distributions, and the bottom rows are volume size distributions. The dashed lines (blue, red, and green) show the integrated number density and volume density in each panel for particle radius from 10^{-3} to 10 μm. *Integrated* means we add the particle number/volume smaller than that radius together to get the value for that radius. For example, for radius 0.1 μm, the modeled integrated volume for the NH is ~ 1.5×10^{-2} um^3/cm^3, which means the volume of all the modeled particles between 0.001 and 0.1 um is ~1.5×10^{-2} um^3/cm^3. Therefore, the value of the dashed lines at 10 μm gives the value of the total number densities or volume densities for particles from 10^{-3} to 10 μm. NH = Northern Hemisphere; SH = Southern Hemisphere; PSCs = polar stratospheric clouds; LOAC = Light Optical Aerosol Counter.

different estimates. Therefore, we conduct a sensitivity case (HalfSO2) with half of the SO_2 emission for Mount Calbuco eruption compared with the Base case. To investigate the PSCs, we conduct a gravity wave case (Base_gw) using random temperature fluctuations with a peak amplitude of ±2 K over major Antarctic mountains (Zhu, Toon, Lambert, et al., 2017) and a case (NoSTStoNAT) without homogeneous nucleation from STS to NAT. We also do a simulation with half the SO_2 emissions on 22 April and half on 23 April, and

Table 2
Model Cases and Their Descriptions

Case name	Case descriptions
Base	Volcanic eruptions in previous years, 0.4 Tg of SO_2 for Calbuco
HalfSO2	Volcanic eruptions in previous years, 0.2 Tg of SO_2 for Calbuco
Noemission	No volcanic eruptions
NoCalbuco	Volcanic eruptions in previous years, no injection from Calbuco
Base_gw	Base case with a random temperature fluctuation of ±2 K
Base_gw_1K	Base case with a random temperature fluctuation of ±1 K
NoSTStoNAT	Base case with no homogenous nucleation from STS to NAT

Note. STS = supercooled ternary solution; NAT = nitric acid trihydrate.

another simulation with 0.4 Tg of SO_2 spread evenly into an area 5 times larger than in the Base case. These two simulations are similar to the Base case and are not discussed further. We also conduct a case (Base_gw_1K) similar to Base_gw but with a random temperature fluctuation with a peak amplitude of ±1 K. We do not show figures on this case because its pattern is very similar to Base_gw, but we will discuss the simulations for this case along with the Base_gw.

3.2. Calculating the Optical Properties

We use the T-matrix approach (Mishchenko & Travis, 1998) to calculate backscatter and extinction coefficients. We assume a refractive index of 1.448 for sulfuric acid aerosol and STS to be consistent with the OMPS aerosol retrieval algorithm (Loughman et al., 2017), 1.5 for NAT and 1.308 for ice (Pitts et al., 2009). We assume NAT and ice to be spheroids with an aspect ratio of 0.9 and 0.95 and STS to be spherical. The wavelengths considered in this approach range from 214 to 2000 nm, which is suitable for the instruments we are interested in this paper (750 nm for OMPS, 675 nm for OSIRIS, and 532 nm for CALIPSO). The optical properties are determined by the refractive index, number density, and radius of the particles and wavelength of the instruments. The sectional model CARMA allows us to calculate the optical properties from computed number densities for various particle sizes rather than assuming an analytic size distribution as is done with the modal aerosol model used with WACCM in Mills et al. (2016).

The extinction or particulate backscatter coefficient is

$$\beta = \sum_{r=r_{\min}}^{r_{\max}} n(r)\sigma(r) = \sum_{r=r_{\min}}^{r_{\max}} n(r)\cdot\pi r^2 Q(r)$$

where, $n(r)$ is the number density of particles with radius r; $\sigma(r)$ is the extinction or backscatter cross section; and $Q(r)$ is the extinction or backscatter efficiency factor.

The Ångström exponent is calculated using the equation:

$$\alpha = -\frac{\ln\frac{\beta_{\lambda 1}}{\beta_{\lambda 2}}}{\ln\frac{\lambda 1}{\lambda 2}}$$

where $\beta_{\lambda 1}$ and $\beta_{\lambda 1}$ represent the extinction coefficient at wavelength $\lambda 1$ and $\lambda 2$, which are determined by the instrument being used to measure the exponent.

4. Model Results

4.1. Aerosol and PSC Size Distributions After the Mount Calbuco Volcanic Eruption

Particle size distributions reflect the formation and evolutionary history of particles. They are often needed in satellite retrieval algorithms to generate optical parameters like phase function and Ångström exponent. The phase function describes the angular distribution of the light after scattering from the particles. The angle between the initial and final light directions is defined as the single-scattering angle (SSA) for the stratospheric aerosols. If the aerosols along the line of sight are optically thin, then the SSA approximates the net distribution of light. Many of the limb scattering satellites apply size distributions based upon a fit to balloon or aircraft data to calculate extinction. However, the size distribution is a function of time and space. The size distribution computed by the model can help to fill in the locations and times that particle counter data are not available and help to identify locations where it would be interesting to have in situ measurements. For example, the phase function is smaller and more variable with particle size for backscatter than for forward scatter. The small backscatter phase function causes signal-to-noise difficulties for the OMPS LP extinction retrieval in the SH where the observational geometry of the satellite is backscattering.

Figure 1 shows the WACCM/CARMA simulated particle volume ($\frac{dV}{d(\ln r)}$) and number ($\frac{dN}{d(\ln r)}$) size distributions from the Base case on 19 August 2015 at 52 hPa, which is ~20 km for Northern Hemisphere (NH) midlatitude and SH in the tropics, and 18 km at high latitude where PSCs form. We compared them with satellite-assumed size distributions in their extinction retrieval algorithm, as well as a measured distribution from the LOAC data at the Reunion Island site at 20 km. In the following paragraphs, we will refer to the bi-mode lognormal size distribution assumed by OMPS (Loughman et al., 2017) as L17 and to the lognormal size distribution assumed

by OSIRIS (Bourassa et al., 2012) as B12. The lognormal size distributions are calculated assuming the total volumes of sulfuric acid aerosol are the same as the model in each case. The volume equations are as follows:

$$\text{Volume} = \int_{r=0}^{\infty} \frac{4}{3}\pi r^3 n(r)\mathrm{d}r$$

where $n(r) = \frac{\mathrm{d}N}{\mathrm{d}r} = \frac{1}{r}\frac{\mathrm{d}N}{\mathrm{d}(\ln r)}$. The size distribution equation for L17 and B12 is

$$\frac{\mathrm{d}N}{\mathrm{d}(\ln r)} = \sum_{i=1}^{m} \frac{N_i}{\sqrt{2\pi}\ln\sigma_i} \exp\left[-\frac{1}{2}\left(\frac{\ln r - \ln r_i}{\ln\sigma_i}\right)^2\right]$$

where m is 2 for L17 and 1 for B12. For L17, r_1 and r_2 are 0.09 and 0.32 μm; σ_1 and σ_2 are 1.4 and 1.6; N_2/N_1 is 0.003. For B12, r_1 is 0.08 μm and σ_1 is 1.6. The size distribution equation for the model is

$$\frac{\Delta N}{\Delta(\ln r)} = \frac{N_{i\text{bin}}}{\text{bin width}} r_{i\text{bin}}$$

$N_{i\text{bin}}$ is number density for each bin; $r_{i\text{bin}}$ is the middle bin size; and bin width is the width between bin size upper boundary and lower boundary. The equation for volume size distribution is

$$\frac{\mathrm{d}V}{\mathrm{d}(\ln r)} = \frac{4}{3}\pi r^3 \frac{\mathrm{d}N}{\mathrm{d}(\ln r)}$$

The WACCM/CARMA modeled size distributions are shown at three locations in Figure 1: The NH midlatitude where the size distribution is close to *background sulfate* (Figures 1a and 1d); the SH Reunion Island site where it is affected by the Mount Calbuco eruption (Figures 1b and 1e); and near the Antarctic region where STS forms (Figures 1c and 1f). Note that the background sulfate here is still affected by the volcanic sulfate aerosol formed in years previous to the Mount Calbuco eruption. In Figures 1b and 1e, both the number and volume size distributions from the model (blue histogram) fit the LOAC observations from Reunion Island site (black circles) within their error bars. We eliminate the particles larger than 1 μm in the LOAC observation because the uncertainties are high when the concentration is lower than 10^{-2} cm^{-3}. The modeled number density of sulfuric acid aerosol in the SH Reunion Island site in 2015 (Figure 1b, blue histogram) is significantly increased relative to background conditions (Figure 1a, blue histogram) due to sulfuric acid aerosol nucleation especially in the size range smaller than 0.06 μm. These numerous small particles are not important for extinction or phase function retrievals in the near infrared but are important to PSC growth and nucleation. The Reunion Island site is at 21°S, in the tropics, so some new particles are due to Upper-Troposphere-Lower-Stratosphere sulfate nucleation. The modeled volume of sulfuric acid aerosol in the SH Reunion Island site of the model (Figure 1e, blue histogram) is about 1 order of magnitude higher and covers a wider size range (0.02 to 2 μm) compared with background sulfate (0.04 to 1 μm) in the NH (Figure 1d, blue histogram). The modeled STS (Figures 1c and 1f) has a narrower size distribution than the modeled background or the modeled volcanic sulfate aerosol, because rapid condensational growth dominates STS microphysics, which tends to narrow the distribution. The modeled STS effective radius is ~ 0.08 μm with a larger number density (~ 100 #/cm^3 shown by the blue dashed line in Figure 1c) than the typical number density inside the polar vortex (~ 10 #/cm^3, Dye et al., 1992). The high number density provides evidence that volcanic sulfate aerosol enters the vortex at least before August and increases the number density, but decreases the effective radius of PSCs. The modeled number density of PSCs is consistent with the number density of the SH sulfate aerosol (~ 100 #/cm^3 shown by the blue dashed line in Figure 1b). Note that the blue dashed line in Figure 1 only counts the number density of particles with radius from 0.001 to 10 μm.

Figure 1 also shows lognormal size distributions that OMPS and OSIRIS used in their extinction retreval algorithums labeled as L17 and B12. We assume the two lognormal size distributions have the same particle volume as the WACCM/CARMA model in each panel in Figure 1. Both of the lognormal size distributions are similar to the simulated background sulfate distribution (Figures 1a and 1d) and consistent with the simulated volcanic sulfate aerosol (Figures 1b and 1e) when the radius $>$ 0.05 μm. The effective radii (summarized in Table 3) of both L17 and B12 (0.14 μm) are generally consistent with the modeled effective radii (0.16 μm for NH and 0.22 μm for SH).

Table 3
The Extinction at 675 and 750 nm Calculated Using the L17, B12, and Modeled Size Distributions in Figure 1 at Three Specified Locations: NH (46°N, 0°E), SH (21°S, 55°E), and PSC (67°S, 245°W)

Extinction 750 nm	NH	SH	PSC
L17	1.75e−4	8.1e−4	8.2e−4
B12	2.2e−4	1e−3	1e−3
Base	2.1e−4	1.3e−3	1e−4
Extinction 675 nm			
L17	1.4e−4	6.6e−4	6.7e−4
B12	1.7e−4	7.9e−4	8e−4
Base	1.7e−4	1.2e−3	1e−4
Ångström exponent			
L17	2	2	2
B12	2.4	2.4	2.4
Base	1.94	1.19	3.58
Effective radius (μm)			
L17	0.14	0.14	0.14
B12	0.14	0.14	0.14
Base	0.16	0.22	0.08
Optical effective radius (μm)			
L17	0.71	0.71	0.71
B12	0.30	0.30	0.30
Base	0.38	0.46	0.22

Note. The Ångström exponent is calculated using the extinction values at 750 and 675 nm in this table. NH = Northern Hemisphere; SH = Southern Hemisphere; PSCs = polar stratospheric clouds.

Table 3 shows the calculated extinction at 675 and 750 nm and the Ångström exponent between these two wavelengths using the modeled size distributions and the satellite-assumed size distributions (L17 and B12) from 19 August at the locations specified in Figure 1. Generally, the differences between the modeled, L17, and B12 extinctions are smaller than a factor of 2 The SH extinction is about 1 order of magnitude higher than the NH extinction. The Ångström exponent between 675 and 750 nm from the model is 1.94 for modeled background sulfate, 1.19 for modeled volcanic sulfate aerosol, and 3.58 for STS. The modeled volcanic sulfate aerosol reduces the Ångström exponent compared to the modeled background sulfate as would be expected since the volcanic sulfate aerosol is larger than the background aerosol.

The consistency of the modeled, L17, and B12 extinctions in Table 3 cannot guarantee the consistency between the modeled extinction and the satellite-retrieved extinctions, because the limb radiance depends on both extinction and phase function. Loughman et al. (2017) state that the uncertainty in the aerosol phase function is one primary source of error in the OMPS aerosol extinction retrieval algorithm. The phase function differences may contribute to the discrepancy of the extinction comparison between the model and the satellite retrievals. Therefore, we show how the different size distributions influence the phase function in Figure 2. Figure 2b shows the phase function for the size distribution by L17 (blue), B12 (red), and the size distribution derived from the model Base case in NH (green), SH (gray solid line), and the PSC (gray dots). The PSC (gray dots) phase function is very different from the other four aerosol phase functions (solid lines) due to the small STS effective radius caused by the volcano, but neither OMPS nor OSIRIS claims to measure PSCs. The largest difference between the modeled NH and SH phase functions and the L17 phase function is about a factor of 2 at 110° SSA, which is about the OMPS SSA from SH midlatitude to the tropics in Antarctic winter. The B12 phase function is between L17 and the modeled values. Figure 2a shows that the phase function varies greatly with particle sizes for SSA $>$ 80°. For example, the phase function changes by about 1 order of magnitude for SSA $>$ 120° when particle sizes change from 0.15 to 0.2 μm. Therefore, even subtle differences between the L17, R12, and modeled size distributions

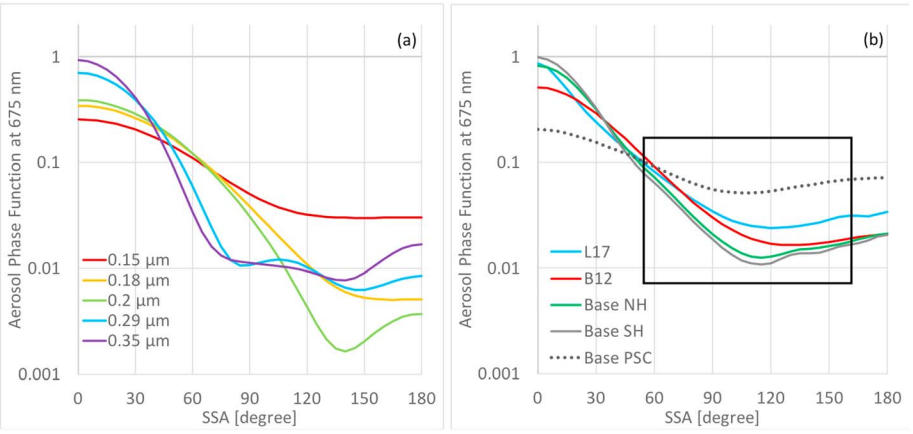

Figure 2. (a) The phase function of monodisperse particles with different sizes at 675 nm as a function of SSA. (b) Aerosol phase function at 675 nm as a function of SSA using the size distributions from L17, B12, and three model cases as shown in Figure 1. The black square indicates the estimated range of SSA that the OMPS and OSIRIS satellites observe between 46°N and 67°S from April to October. The OMPS SSA approximately ranges from 70° to 120°, and OMPS SSA approximately ranges from 60° to 160°. SSA = single-scattering angle; OMPS = Ozone Mapping and Profiler Suite; OSIRIS = Optical Spectrograph and InfraRed Imager System; NH = Northern Hemisphere; SH = Southern Hemisphere; PSC = polar stratospheric cloud.

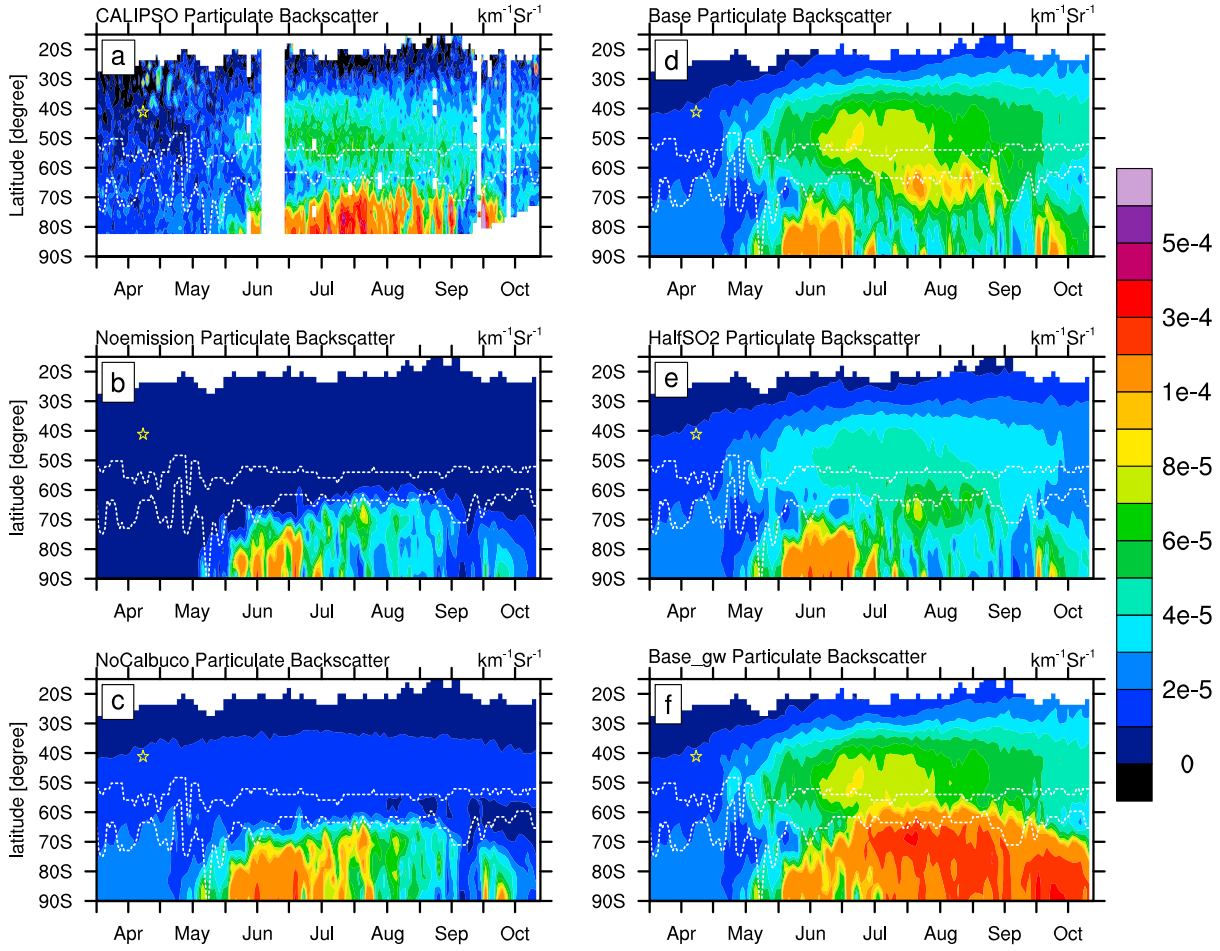

Figure 3. The zonal average particulate backscatter coefficient from CALIPSO L1B data and calculated from the model cases at 16 km (~100 hPa). The white dashed lines indicate the latitude range over which the polar vortex edge is located on each day. The yellow stars indicate the location and time of the Mount Calbuco eruption. CALIPSO = Cloud-Aerosol Lidar and Infrared Pathfinder Satellite Observations.

and effective radii can result in inconsistent phase functions. Another reason for sensitivity to the limb scattering function is that when we calculate the optical effective radius, the extinction coefficient adds weight to the larger sizes. We calculate the optical effective radius using the equation: $\text{Reopt} = \frac{\int Q\text{ext} \cdot n(r) r^3 dr}{\int Q\text{ext} \cdot n(r) r^2 dr}$ in Table 3. By adding the extinction coefficient (*Q*ext) to the effective radius calculation, the large particles become more important due to their large extinction coefficient. As shown in Table 3, the L17 optical effective radii are much larger than other cases, and the differences between each case are more obvious than when considering the effective radius. Therefore, we conclude that large particles can significantly affect the aerosol phase function depending on the large particle number density. The scarcity of information on large particle number density adds to the challenges faced by satellites in their retrieval of extinction.

4.2. Aerosol and PSC Optical Properties Compared With CALIPSO, OMPS, and OSIRIS

In this section, we compare the optical properties calculated from the WACCM/CARMA model with the CALIPSO, OMPS, and OSIRIS observations in the Antarctic winter of 2015. We first show the backscatter of the sulfuric acid aerosol from both simulations and CALIPSO observations after the eruption and discuss how the volcanic cloud progresses toward the Antarctic region from April to October (Figure 3). The modeled number density and effective radius are also shown to provide evidence of the influence of the volcanic eruption on the sulfate aerosol and PSCs inside the polar vortex (Figures 4 and 5). We also compare the zonal average optical properties calculated from simulations with satellite observations to view the vertical extent of the volcanic sulfate aerosol and PSCs in May (Figure 6), July (Figure 7), and September (Figure 8). The

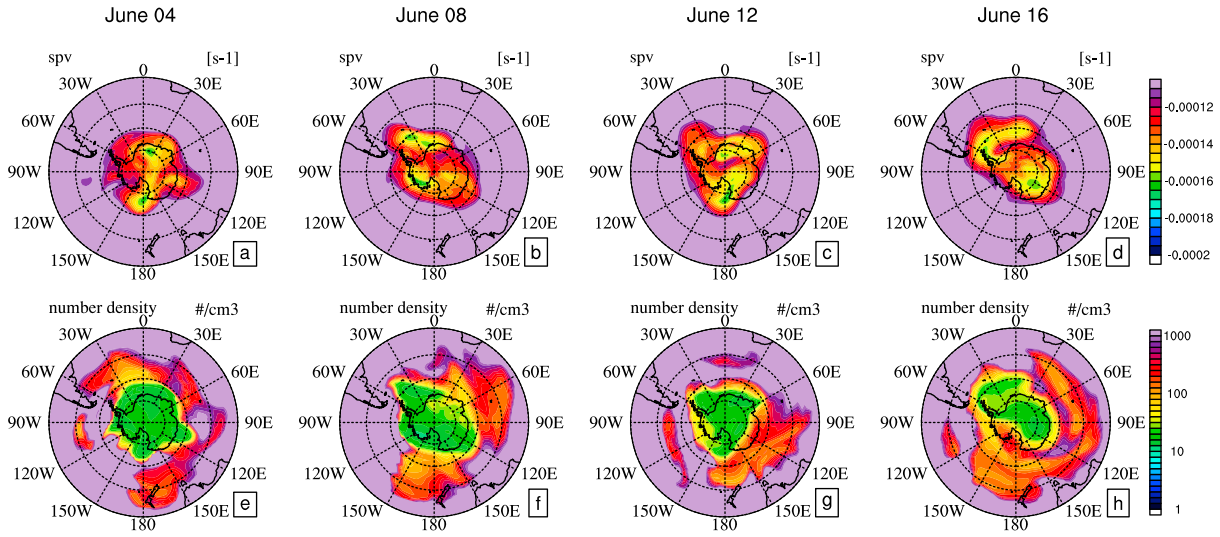

Figure 4. The sPV (top panels) and the sulfuric acid aerosol number density (bottom panels) from 4 June to 16 June at 100 hPa from the Base case. sPV = scaled potential vorticity.

reasons to show these three periods are that the surface area of sulfate aerosol and PSCs inside the vortex in May and September is the most important for ozone chemistry because the Antarctic region is not completely dark then, while July is a good month to analyze the large amount of PSCs as well as transport of volcanic sulfate aerosol.

Figure 3 shows the zonal average backscattering ratio from CALIPSO compared with the model cases with and without the Mount Calbuco eruption from April to October. The figure shows how the volcanic sulfate aerosol progresses toward the South Pole at 16 km (~100 hPa). The white dashed lines indicate the latitude range over which the edge of the polar vortex is located on each day, as defined using the method described by Harvey et al. (2002). The CALIPSO data are interpolated to the WACCM model grid. CALIPSO particulate backscatter is calculated using the L1B total attenuated backscatter minus the Rayleigh backscatter calculated from our model. Compared with the Noemission (Figure 3b) and NoCalbuco (Figure 3c) case, the

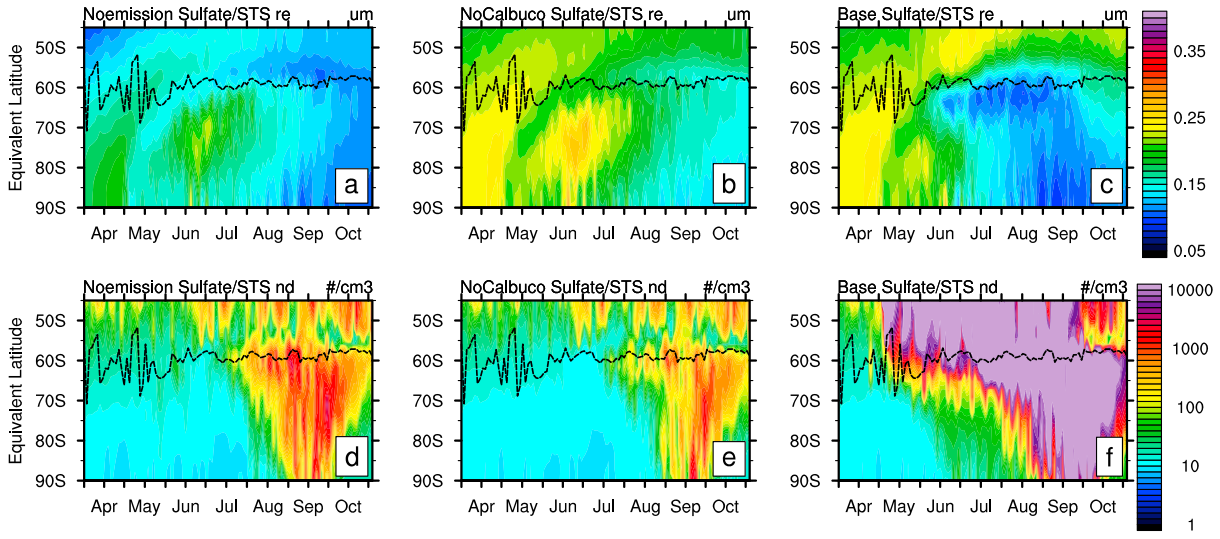

Figure 5. The effective radius (top panels) and number density (bottom panels) of sulfuric acid aerosol and STS as a function of time and equivalent latitude from Noemission case (left), NoCabuco case (middle), and Base case (right) at 16 km. The black dashed lines indicate the polar vortex edge equivalent latitude. STS = supercooled ternary solution.

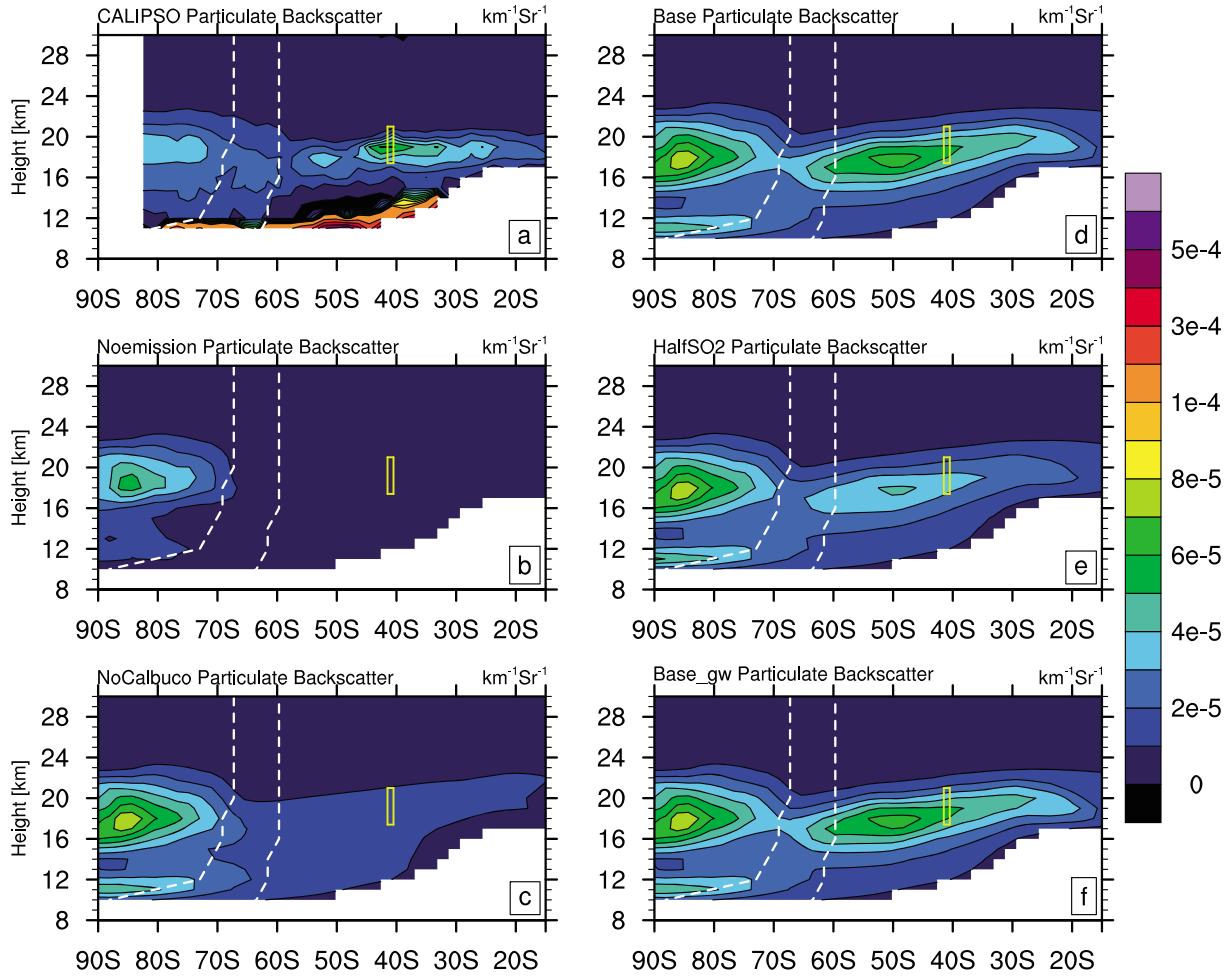

Figure 6. The (a) CALIPSO particulate backscatter from 21 to 29 May 2015 compared with modeled cases: (b) Noemission, (c) NoCalbuco, (d) Base, (e) HalfSO2, and (f) Base_gw. The figures are 9-day zonal averages. The white dashed lines indicate the latitude range over which the polar vortex edge is located during this time. The yellow boxes indicate the SO_2 injection latitude and height from Mount Calbuco eruption in the model. CALIPSO = Cloud-Aerosol Lidar and Infrared Pathfinder Satellite Observations.

Base case (Figure 3d) shows an enhanced backscatter outside the vortex and south of 30°S that peaks in June and July, consistent with the CALIPSO observation. Figures 3a and 3d indicate the CALIPSO and modeled volcanic sulfate aerosol reach the latitudes within the vortex edge ranges in May. These particles are very important to the polar chemistry thereafter. The backscatter of the Base case (Figure 3d) in southern midlatitudes is about 2×10^{-5} km^{-1}/sr higher than CALIPSO (Figure 3a), while the midlatitude backscatter of the HalfSO2 (Figure 3e) case is about 2×10^{-5} km^{-1}/sr lower than CALIPSO, indicating that the injected mass lies between 0.2 and 0.4 Tg. Inside the vortex, the Base case shows an elevated backscatter starting in June, indicating that the sulfuric acid aerosol and PSCs are enhanced by the volcanic sulfate aerosol transported from the Mount Calbuco eruption. None of the model cases capture the large backscatter between June and September near the South Pole, indicating that too few PSCs form during these periods in the model. The small PSC backscatter is very likely due to the overdenitrification in early winter as we will discuss in section 4.3. The model cases including gravity waves (Base_gw in Figure 3f and Base_gw_1K not shown), known to occur over the Antarctic Peninsula, overestimate the latitudinal extent of PSCs.

To further explore how the aerosol progresses into the vortex, we investigate the shape of the vortex and the number density and effective radius of volcanic sulfate aerosol and PSCs. Figure 4 shows the scaled potential vorticity (sPV, Dunkerton & Delisi, 1986; Manney et al., 1994) and modeled sulfate number density from the Base case. sPV is calculated using the Modern Era Retrospective Analysis for Research and Applications version 2 horizontal winds and temperatures. In Figure 4, we can see the shape of the vortex

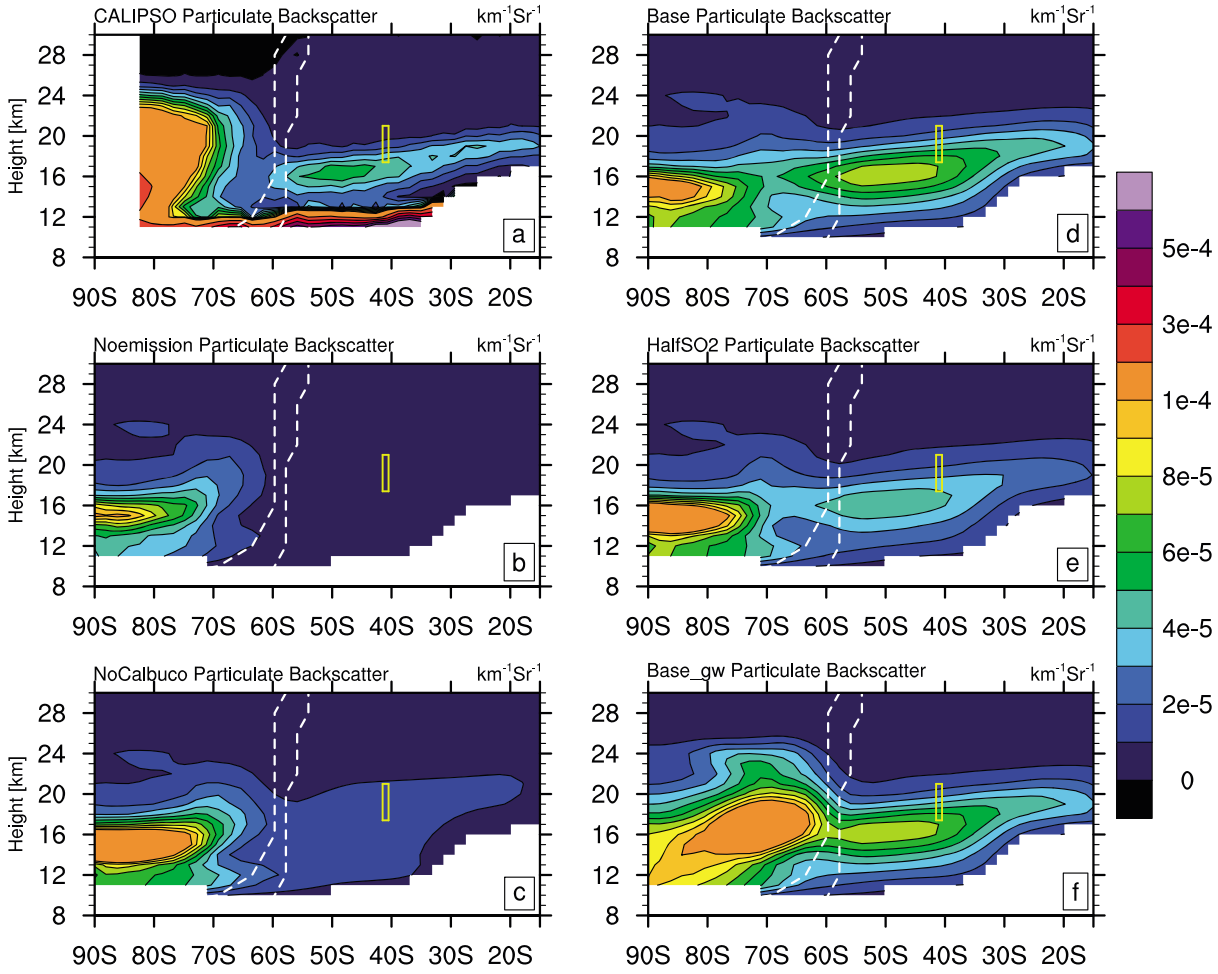

Figure 7. As Figure 6 but 20-day zonal averages from 30 June to 18 July 2015. CALIPSO = Cloud-Aerosol Lidar and Infrared Pathfinder Satellite Observations.

(approximated here by the -0.00011 s^{-1} sPV contour coincident with dark purple in Figure 4a) matches the shape of the green areas in the number density for all the simulated particle plots (Figure 4e) on 4 June. Green areas show low sulfate aerosol number density of about 20 cm^{-3}. On 8, 12, and 16 June, there are tongues of high number density of sulfate aerosol (Figures 4f–4h) near 30°E, 150°W, and 30°E longitude that penetrate the vortex edge (Figures 4b–4d) due to poleward planetary wave breaking processes. This air is rapidly transported into the vortex core and irreversibly mixed.

In Figure 5, we show the effective radius and number density of sulfuric acid aerosol and STS (no NAT or ice) for the three model cases: Noemission, NoCalbuco, and Base. Because of the distorted shape of the vortex as seen in Figures 4a–4d, we average the number density and effective radius to the equivalent latitude instead of the geographic latitude. The equivalent latitude encloses the same sPV area as the latitude circle of equivalent value. The black dashed line in Figure 5 is the modeled equivalent latitude of the polar vortex edge computed using the method described by Harvey et al. (2002). Comparing the Noemission (Figures 5a and 5d) case with the NoCalbuco case (Figures 5b and 5e) shows that previous volcanic eruptions increase the effective radius by ~ 0.05 μm but do not affect the number density very much. Coagulation plays an important role to reduce the volcanic sulfate aerosol number density in the previous years to the background level. The increased effective radius may change the coagulation kernel, so the number density of the NoCalbuco case is slightly smaller than the Noemission case. Comparing the NoCalbuco case and the Base case (Figures 5c and 5f) shows that the Mount Calbuco eruption increases the number density by at least 2 orders of magnitude outside the vortex after the eruption in late April, and it increases the number density inside the vortex by at least 1 order of magnitude after mid-June, indicating that the Mount Calbuco eruption causes abundant

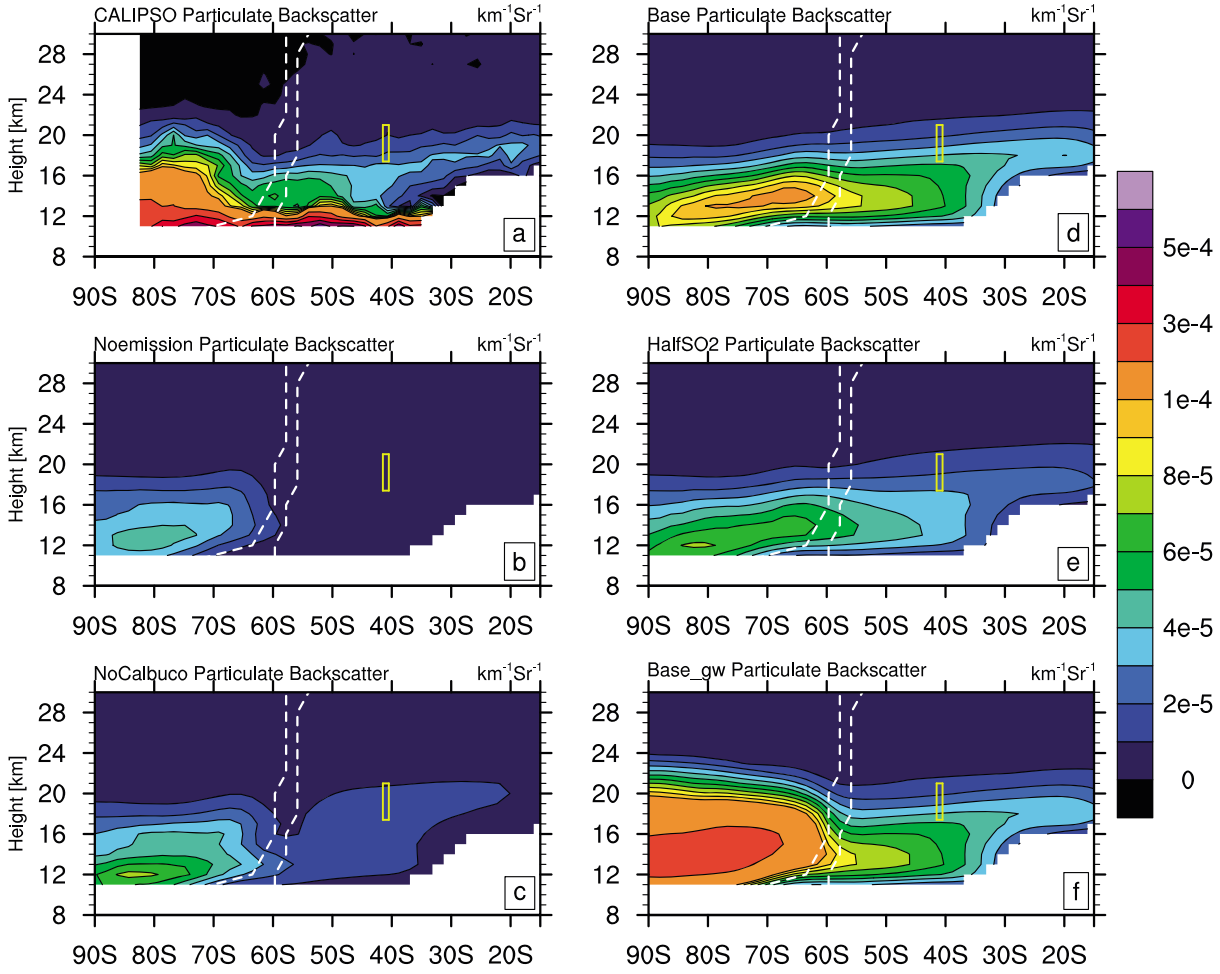

Figure 8. As Figure 6 but 15-day zonal averages from 31 August to 14 September 2015. CALIPSO = Cloud-Aerosol Lidar and Infrared Pathfinder Satellite Observations.

sulfuric acid aerosol nucleation. In contrast, the Mount Calbuco eruption increases the effective radius by ~ 0.05 μm outside the vortex but decreases the effective radius inside the vortex. Outside the vortex, the increased sulfate burden and coagulation cause the increase of the effective radius; while the effective radius decreases inside the vortex due to extensive newly nucleated sulfate particles penetrating into the vortex and competing with each other for HNO_3 vapor to grow into PSCs.

Figures 6–8 show the vertical structure of the backscattering ratio from CALIPSO and from five model cases: Noemission, NoCalbuco, Base, HalfSO2, and Base_gw. The white regions in the plots indicate that the altitude is below the tropopause in the model or denote missing CALIPSO observations. The dashed lines indicate the range of latitudes over which the polar vortex edge is identified, as defined in previous figures.

Figure 6 shows particulate backscatter during a typical period in late May when STS and NAT start to form in the Antarctic area, but when it is not cold enough to form ice. The CALIPSO data (Figure 6a) shows two areas of high backscatter at 16–20 km: one is near 40°S and another one is near the South Pole. The Base case (Figure 6d) also shows high backscatter near the South Pole, but the high backscatter at midlatitudes is close to 50°S instead of 40°S as seen by CALIPSO. In the midlatitudes, the peak value from the Base case is close to the CALIPSO observations. The HalfSO2 case (Figure 6e) reduces the backscatter outside the vortex, and the peak value is lower than CALIPSO by ~ 2×10^{-5} km^{-1}/sr^{-1}. In the Noemission case (Figure 2b), the model shows very low backscatter in midlatitudes and the backscatter near the South Pole is weaker than other model cases, indicating that the previous volcanic sulfate aerosols enhance the backscatter from sulfate aerosols and PSCs. The Base_gw cases (Figure 6f) and Base_gw_1K case (not shown) do not show enhanced backscatter in this time period because ice PSCs have not formed. Near the tropopause,

CALIPSO shows very high backscatter, which is probably due to tropospheric clouds that we do not simulate in CARMA.

Figure 7a shows the strong midwinter particulate backscatter near the South Pole due to PSCs in CALIPSO observations. The PSC backscatter near the South Pole in Noemission case (Figure 7b) has the smallest value among all cases. The NoCalbuco case (Figure 7c) strongly enhances the PSC backscatter and slightly increases the backscatter from sulfate aerosols in midlatitude. It is interesting to note that the PSC backscatter from the Base case is smaller than in the HalfSO2 case, and the backscatter in the HalfSO2 case is smaller than in the NoCalbuco case at this period of time. The lower value for the Base case is probably due to the newly nucleated sulfate aerosol from the Mount Calbuco eruption penetrating the vortex and competing for HNO_3 gas. However, none of the simulations reproduce the large backscatter in July near the South Pole above 16 km (Figure 7c). This error is very likely due to the strong denitrification that occurred in early winter in the model, as discussed further in the next section. The Base_gw case (Figure 7f) does enhance the PSCs formation, but the region of enhancement extends too far toward the edge of the vortex and not high enough from 70 to 80°S. Reducing the temperature fluctuation (Base_gw_1K, not shown) reduces the backscatter enhancement near the edge of the vortex, but the backscatter is still higher than in the observation. At midlatitude, the model Base case (Figure 7d) captures the midlatitude backscatter around 16 km, though perhaps the computed backscatter is about 2 times too large. Again, the backscatter in the HalfSO2 case (Figure 7e) is slightly lower than the CALIPSO observation. Comparison between Figures 6a and 7a shows that the peak midlatitude backscatter from the volcanic sulfate aerosol is observed to descend about 4 km as it moves from ~ 40°S to ~ 50°S. The Base case shows a similar downward tilt, but the peak backscatter at 50°S is already established in May (Figures 6c and 7c).

Figure 8 shows the backscatter in September, when large ozone loss begins. At this time, the Noemission case (Figure 8b), NoCalbuco case (Figure 8c), the Base case (Figure 8d), and the HalfSO2 case (Figure 8e) show too little backscatter between 14 and 18 km south of 70°S compared with CALIPSO (Figure 8a). In contrast, the Base_gw (Figure 8f) show too much backscatter above 16 km throughout the vortex. Reducing the temperature fluctuation (Base_gw_1K, not shown) reduces the backscatter value, but it is still higher than the CALIPSO observation. The particulate backscatter in the NoCalbuco case near the South Pole is much lower than the Base case. In September, the PSCs start to fade away due to the increase of the temperature. At the same time, most of the volcanic aerosol from the Mount Calbuco eruption enters the polar vortex and enhances the backscatter. Again, the peak values observed by CALIPSO near 65°S and 14 km are between the Base case and the HalfSO2 case, but the volcanic sulfate aerosol layer observed by CALIPSO has a narrower vertical extension than these two model cases. All three figures (Figures 6–8) show that the volcanic sulfate aerosol influences latitudes poleward of 20°S. At 20°S, the volcanic sulfate layer is around 20 km at which we showed the size distribution in Figure 1.

From the backscatter in the three periods shown above, we conclude that the volcanic sulfate aerosol in midlatitude is between the Base case and the HalfSO2 case. The amount of SO_2 emitted into the stratosphere is between 0.2 and 0.4 Tg. The volcanic sulfate aerosol previous to the Mount Calbuco eruption increases effective radius and enhances the backscatter compared with simulations without these eruptions. The sulfate aerosol enhanced by the additional SO_2 injection from the Mount Calbuco eruption descends in altitude over time as it is slowly transported toward the Antarctic. Part of the newly nucleated sulfate aerosol enters the polar vortex due to poleward planetary wave breaking processes and reduces the effective radius of PSCs. The modeling of PSCs still needs to improve. Adding gravity waves enhances the PSCs, but not always in the right area. As discussed by Zhu, Toon, Lambert, et al. (2017), our gravity wave parameterization is very simple. Using more sophisticated gravity wave parameterizations is the subject of future work.

The Ångström exponent is often used to convert extinctions to the same wavelength for satellite data intercomparison. However, using a fixed Ångström exponent can introduce errors, as we show in Table 3, the volcanic aerosol shows a lower Ångström exponent (1.19) than the background sulfate aerosol (1.94) from our model calculation. Instead of using the Ångström exponent to convert the OMPS extinction to the OSIRIS wavelength, for example, we calculate the modeled extinction at 675 and 750 nm, so that we can compare OMPS and OSIRIS extinction indirectly to each other but directly to the model. Figure 9 compares the monthly average extinction coefficient in September from OSIRIS at 750 nm and OMPS at 675 nm and the modeled extinction from the Base case and the HalfSO2 case at these two wavelengths.

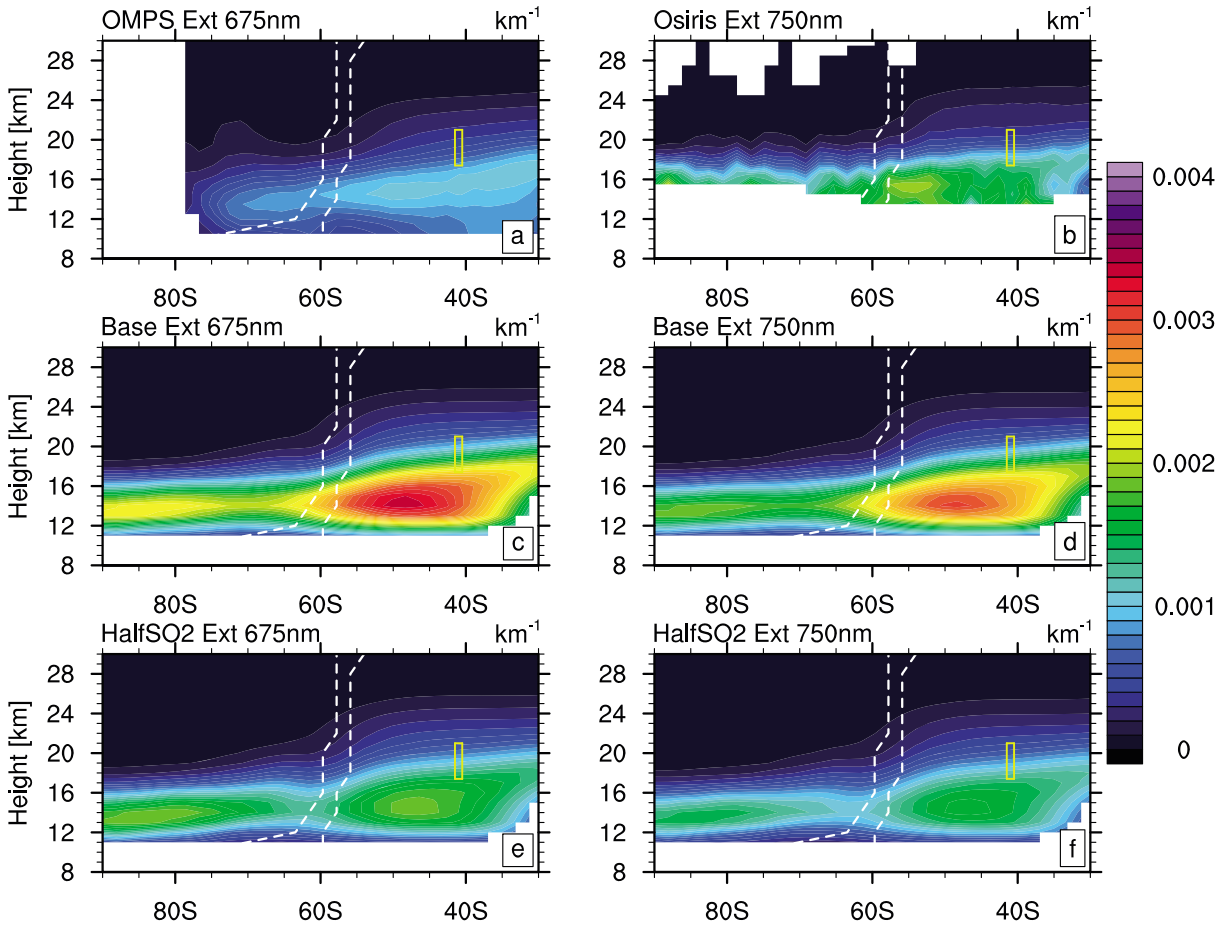

Figure 9. The modeled extinction coefficient compared with OMPS 675 nm and OSIRIS 750 nm retrieved extinction in September 2015. OMPS = Ozone Mapping and Profiler Suite; OSIRIS = Optical Spectrograph and InfraRed Imager System.

The Base case (Figure 9d) simulated extinction is about 2 times larger than OSIRIS extinction (Figure 9b). The extinction of HalfSO2 case (Figure 9f) is slightly lower than OSIRIS. This is consistent with the backscatter comparisons show that the backscatter in SH midlatitude from CALIPSO is between the base case and the HalfSO2 case. The largest values of OSIRIS extinction are at about 55°S and 15 km altitude, but the modeled peak extinction is about 10°N of the peak of the OSIRIS extinction. Part of the model-OSIRIS discrepancies may be due to biases in OSIRIS extinction that saturates above a certain threshold likely reached in volcanic conditions (Lurton et al., 2018). These authors reported that the comparisons between WACCM/CARMA simulations and OSIRIS observations dramatically improved when OSIRIS biases were taken into account. The shape of the OMPS extinction distributions suggests descent from midlatitudes to 80°S. This is also seen in the OSIRIS data and modeled results, but the extinction of OMPS (Figure 9a) is about half of the HalfSO2 case value (Figure 9e) and a third of the Base case value (Figure 9c) near 50°S and 15 km altitude. We note that Bègue et al. (2017) show the OMPS extinction compares reasonable well with ground lidar results, but they use the OMPS version 0.5 aerosol product, while we use the version 1 product in this paper.

From the comparisons of backscatter and extinction above, we conclude that both OSIRIS and CALIPSO observations are between the Base case and the HalfSO2 case. Therefore, CALIPSO and OSIRIS are consistent with each other in September 2015. The SO_2 emission into the stratosphere is between 0.2 and 0.4 Tg. The OMPS extinction is underestimated by about a factor of 2 relative to OSIRIS. Loughman et al. (2017) list the uncertainties of OMPS due to radiative transfer limitations in order of priority: aerosol scattering phase function, line-of-sight variation in atmospheric properties, and approximate treatment of the diffuse upwelling radiance. In addition, the uncertainties can also be caused by aerosol signals close to the noise level in the

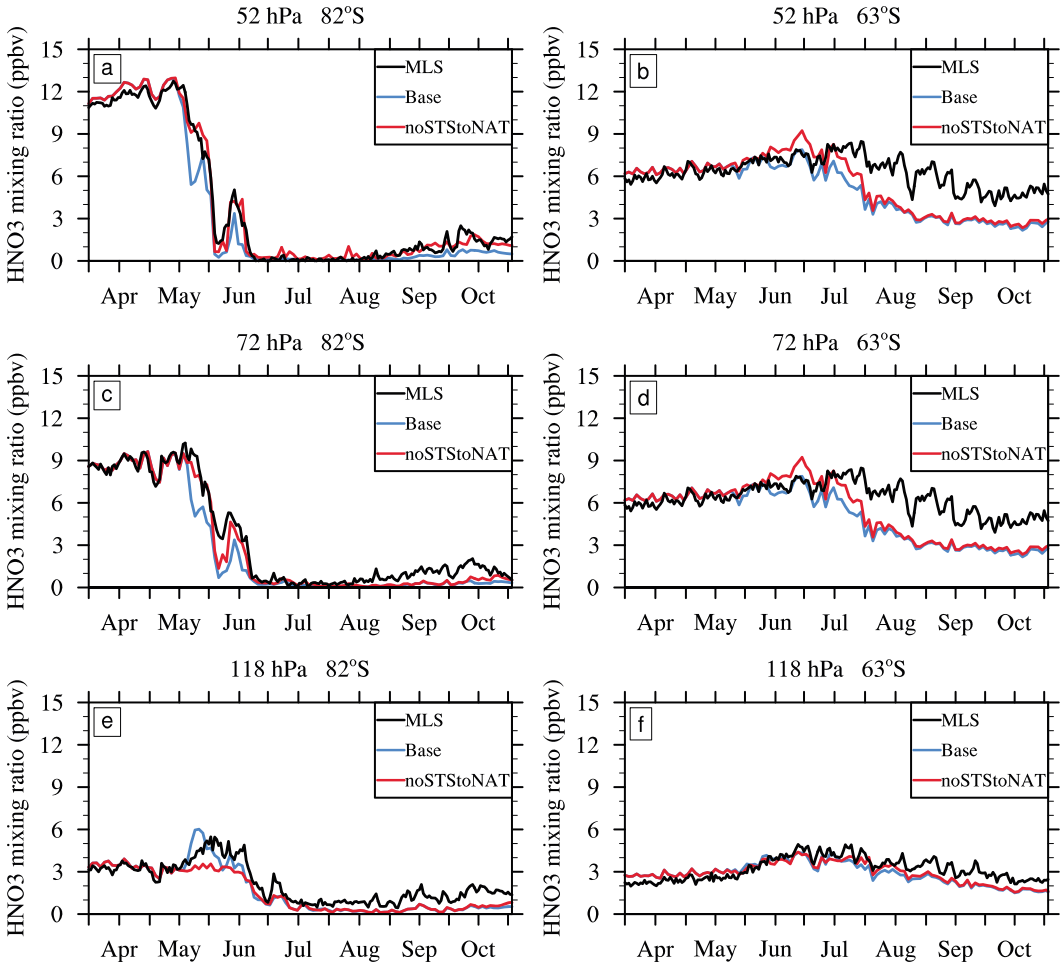

Figure 10. The modeled HNO_3 evolution during 2015 Antarctic winter at 82°S and 63°S compared with MLS observations (black). MLS = Microwave Limb Sounder.

SH, ozone correction errors, aerosol extinction exceeding the algorithm allowed value, the cloud detection algorithm, and poor algorithm convergence in certain circumstances (Loughman et al., 2017). All these factors can contribute to the underestimation of the extinction in Figure 9.

4.3. Denitrification

Denitrification promotes ozone depletion by limiting the amount of NO_y that can be reformed in spring. NO_y removal retards the deactivation of halogen-based compounds (Toon et al., 1986). Figure 10 shows the HNO_3 evolution from MLS observations and two model cases: the Base and the not previously discussed noSTStoNAT. Figure 10 shows two main problems with the modeled denitrification. First, at 82°S, the modeled HNO_3 in the Base case is lower than the observations in late May when PSCs start to form, and in September and October when PSCs disappear. From the PSC backscatter in Figures 3 and 7, we know that the modeled PSC backscatter is smaller than observed by CALIPSO in midwinter. These facts tell us that the early irreversible denitrification in late May is too strong in the model. We also conducted denitrification tests for several other model cases (not shown) including Noemission, NoCalbuco, HalfSO2, and Base_gw, and they all show similar overdenitrification patterns as the Base case. Since the formation of large NAT particles from STS is the major source of denitrification, we turned off this mechanism in the test case noSTStoNAT. In the noSTStoNAT case, the NAT only forms from ice PSCs. In late May, the decrease of HNO_3 in the noSTStoNAT case is only due to the uptake of HNO_3 by STS. Figures 11b and 11e show an example of the PSCs formed in late May in the noSTStoNAT case. They show large backscatter and no depolarization during 25 to 29 May at 52 hPa, which indicates no NAT or ice formed. This case does improve the modeled

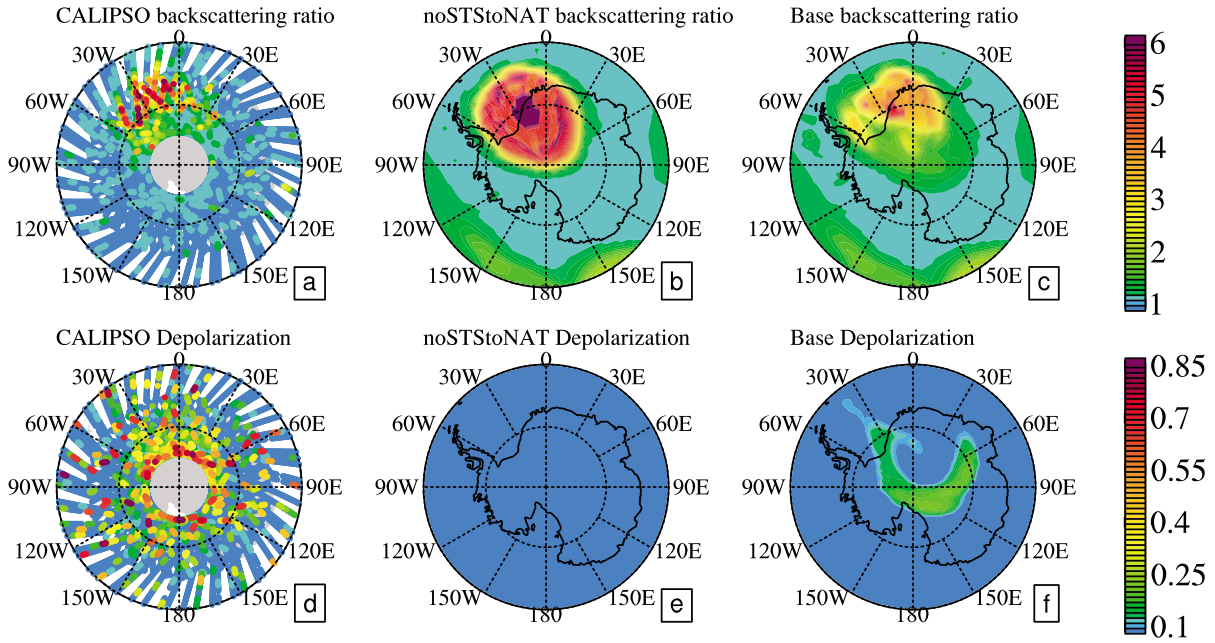

Figure 11. Polar view of backscattering ratio and depolarization at 52 hPa averaged over 25–29 May from CALIPSO (left column) and two model cases: noSTStoNAT (middle column) and Base case (right column). The CALIPSO data use the L2 PSC mask data. CALIPSO = Cloud-Aerosol Lidar and Infrared Pathfinder Satellite Observations; PSC = polar stratospheric cloud.

HNO_3 compared with MLS especially at 52 hPa. But ignoring the formation of NAT from STS is not the proper solution because the combination of CALIPSO and MLS data always show evidence of large NAT particles in late May (Lambert et al., 2012; Zhu, Toon, Pitts, et al., 2017). Both of these papers report the MLS observed rapid gas phase HNO_3 depletion near 20 km in late May, while CALIPSO shows small backscatter but large depolarization at the same region. Figure 11 shows the CALIPSO L2 PSC data in late May compared with the Base case and the noSTStoNAT case simulations. CALIPSO observations have more sparkly dots (especially the depolarization) than both model cases due to the noise. We do not add the calculated noise described in Zhu, Toon, Lambert, et al. (2017) in the model cases. The noSTStoNAT case (Figure 11b) overpredicts the backscatter downwind of the Antarctic Peninsula (60°W to 0°E, 70–80°S). CALIPSO (Figure 11d) observes significant depolarization over Antarctica south of 75°S, as does the Base case from 30°E to 30°W (Figure 11f). However, the noSTStoNAT case does not produce depolarizing particles (Figure 11e) near 75–80°S. As we mentioned in Zhu, Toon, Lambert, et al. (2017), the nonsulfate materials in the stratosphere (e.g., micrometeoroids and volcanic ashes) can serve as the nuclei for heterogeneous nucleation, which may improve the calculated nucleation rate of STS to NAT.

The second problem with modeled denitrification shown in Figure 10 is that the HNO_3 at 63°S is about 1–3 ppbv smaller than the observed abundance from mid-July until the end of the season. The 63°S is a difficult area to simulate because it is near the edge of the vortex as shown in Figures 3 and 6–8, where the temperature gradient is large. Also, the Antarctic Peninsula is located near 63°S and triggers a lot of PSC nucleation. From Figure 7, we find that PSCs occur in the simulations at the edge of the vortex (near 60°S) in midwinter, while CALIPSO does not show very strong backscatter there. One of the possible reasons for this discrepancy is that orographic gravity waves that form over the Antarctic Peninsula (located near 63°S) in our model result in too much NAT formation from either STS or ice.

4.4. Ozone

In this section, we explore the influence of volcanic sulfate aerosol on polar ozone and compare with several results from Solomon et al. (2016) who used the WACCM-CCMI model. As mentioned previously, the WACCM-CCMI simulation shown in this work uses aerosol properties (e.g., sulfate SAD) that are consistent with Mills et al. (2016), not those specified by CCMI) and applied in the study by Solomon et al. (2016). In this section we compare the surface area from our model simulations with those from the WACCM model

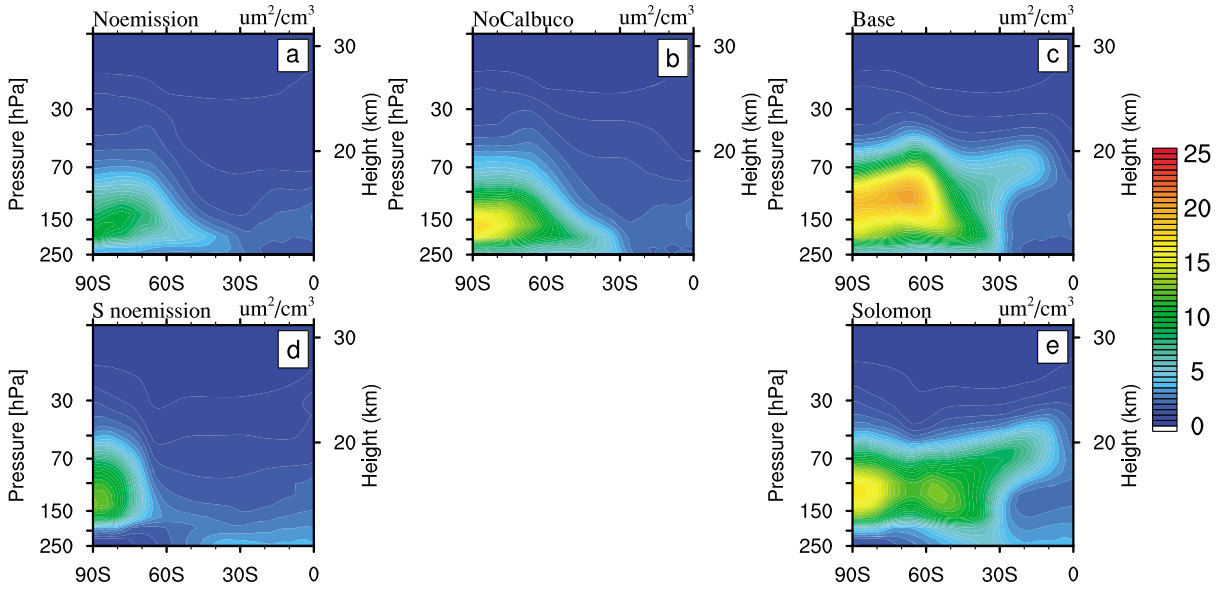

Figure 12. The surface area density (SAD) in September from Noemission case, NoCalbuco case, Base case, and the cases with (labeled as Solomon) and without (labeled as S noemission) volcanic eruptions from Solomon et al. (2016). The figure only shows the sulfuric acid aerosol/STS SAD because both NAT and ICE SAD in our model are below 1 um^2/cm^3. The Solomon et al. (2016) also has NAT SAD lower than 1 um^2/cm^3, but the ICE SAD is high below 150 hPa because it simulates the cirrus cloud near the tropopause. We do not show the NAT and ICE SAD from Solomon et al. (2016) in Figure 12. STS = supercooled ternary solution; NAT = nitric acid trihydrate.

computed using an empirical parameterization for PSCs (Wegner et al., 2012) and a modal model for volcanic sulfate aerosol. We also compare the MLS observed ozone at midlatitudes and near the South Pole with the modeled cases.

The heterogeneous chemistry occurring on the surface of sulfate aerosol and PSCs is very important for chorine activation. Figure 12 shows the SAD of sulfate aerosol and STS in September used in Solomon et al. (2016) with (labeled as Solomon) and without (labeled as S noemission) volcanic eruptions, the Noemission case, the NoCalbuco case, and the Base case. We do not show the NAT SAD because it is relatively small in both our model and Solomon et al. (2016). Wegner et al. (2012) state that the ICE SAD is not important because heterogeneous chemistry on other PSC/aerosol types is fast enough to activate enough chlorine before ICE PSC forms. The NoCalbuco case (Figure 12b) shows an enhanced SAD south of 60°S compared with Noemission case (Figure 12a), indicating the effect of previous eruptions on SAD in September 2015. The Base case (Figure 12c) shows an additional enhanced SAD north of 60°S compared with Noemission case and NoCalbuco case, indicating the Mount Calbuco eruption provides additional surface area from volcanic sulfate as well as enhancing the PSC SAD in the Antarctic. The surface area from Base case and the Solomon case (Figure 12e) shows the sulfate/STS SAD from 200 hPa to 70 hPa extending from the South Pole to about 20°S. The SAD from the base case and the Solomon case are twice as large as the Noemission cases and cover a much larger geographic area from the South Pole to ~ 20°S. The Solomon's noemission case (Figure 12d) shows a slightly higher SAD (~ 2 um^2/cm^3) than the Noemission case near 90°S and 100 hPa, but the SAD from the Noemission case extends to a lower latitude. This difference may contribute to the differences of the ozone hole prediction between Solomon's simulations and our model simulations.

Figure 13 shows the ozone evolution from MLS (black) and two model cases: Noemission (green) and Base (red). The blue shades are the MLS error bars as described in Table 1 (Livesey, 2015). The error bar used in Figure 13 is 0.2 ppmv for 52 hPa, 0.05 ppmv +5% of ozone values for 72 hPa and 118 hPa. The Base case shows a lower ozone amount than the Noemission case at all pressure levels, indicating the effect of volcanic sulfate aerosol from Mount Calbuco and volcanos from the previous years on the ozone depletion. However, the absolute differences between the two model cases are very subtle, less than 0.1 ppmv at all pressure levels. Compared with MLS, the Base case lines are all within the error bars at 82°S. At 63°S, the Base case

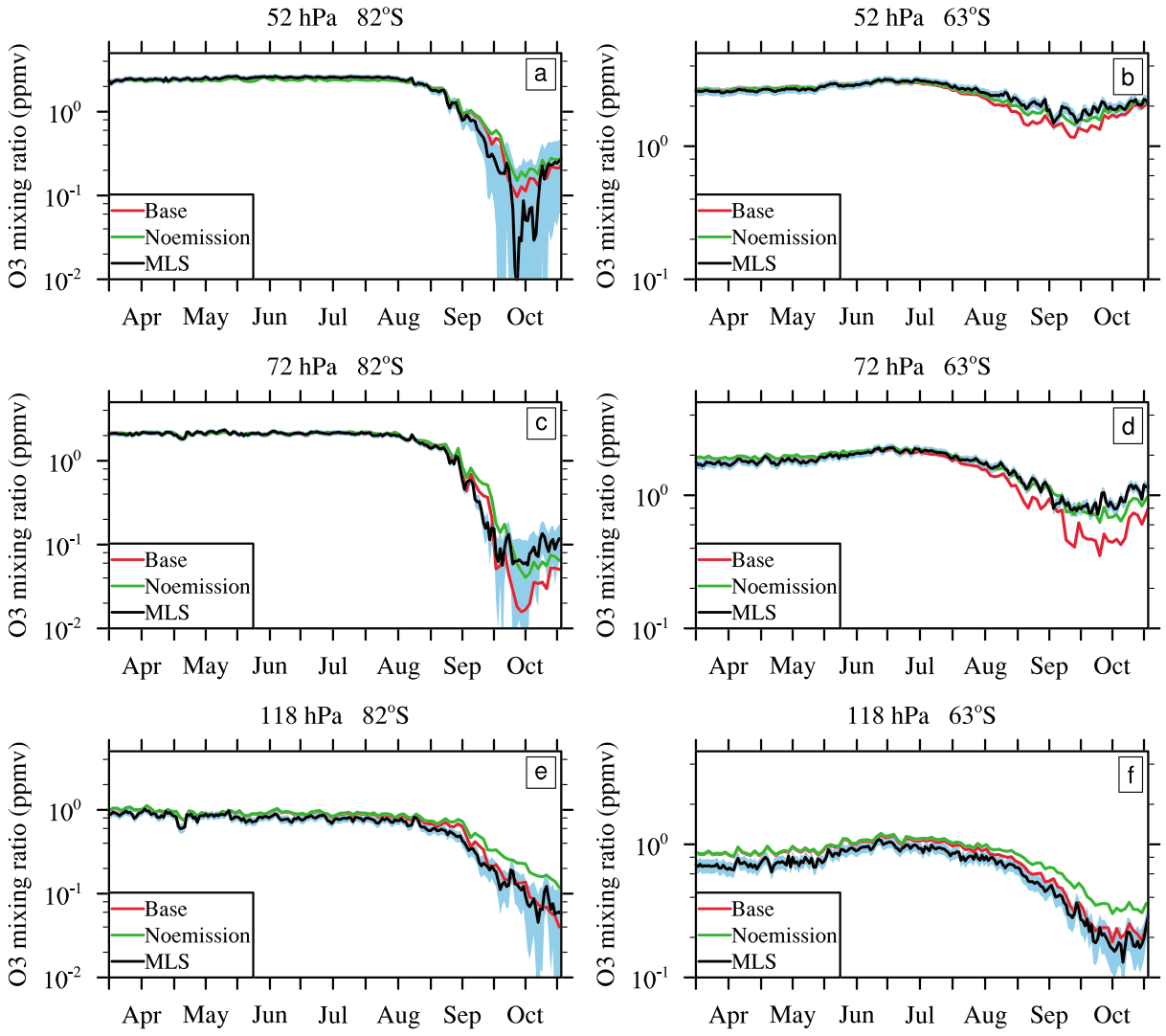

Figure 13. Ozone evolution at 82°S and 63°S from April to October in 2015 from MLS and two model cases: Base and Noemission. The blue shades are the MLS error bars: 0.2 ppmv for 52 hPa, 0.05 ppmv +5% of ozone values for 72 and 118 hPa. The *Y* axis values are different for 82°S and 63°S.

overestimates the ozone depletion slightly compared with the MLS at 52 and 72 hPa but fits MLS perfectly at 118 hPa.

Figure 14a shows the ozone hole area from Total Ozone Mapping Spectrometer/Ozone Monitoring Instrument (TOMS/OMI) observations (black, Solomon et al., 2016), Base case (red solid line), Noemission case (red dashed line), NoCalbuco case (red dotted line), Solomon et al. (2016) with emissions (green solid line), and without emissions (green dashed line). The ozone hole area is defined as the region where total column ozone amount is less than 220 DU. The start of the ozone hole is the first date of an ozone hole that is larger than 12 million km^2 (Solomon et al., 2016). Our model indicates the start date of the ozone hole advanced due to the volcanic eruptions. With the volcanic eruptions, the ozone hole exceeds 12 million km^2 on 5 September in the Base case. The start date shown in the Solomon case is 2 September and in TOMS/OMI, 3 September. In contrast, the start date of ozone hole for the NoCalbuco case is 8 September and for Noemission case is 12 September. Compared with the two cases without volcanic eruptions, our Noemission case shows an obvious delay of ozone hole opening than the Solomon noemission case. This difference might be attributed to the SAD differences as we shown in Figures 12a and 12d. We need to have a detailed analysis on ozone-related chemicals to find the reasons in the future. The average difference between the Base case and the Noemission case in September is 4.9 million km^2, which is consistent with

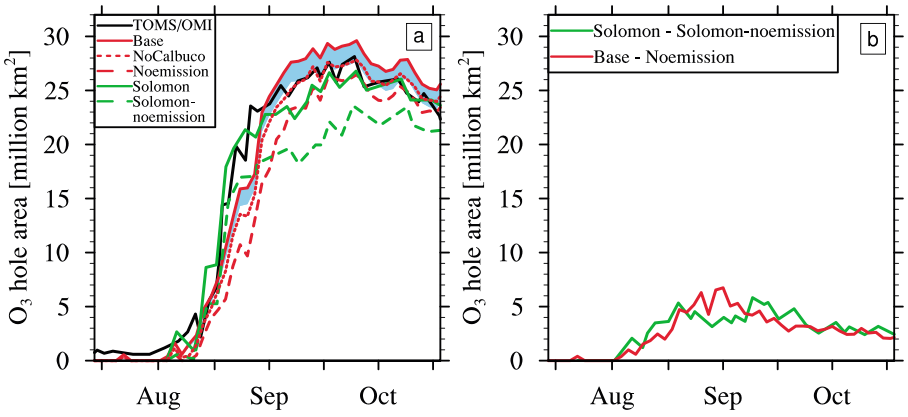

Figure 14. (a) The ozone hole areas (defined as the region where total ozone amount is less than 220 DU) during 2015 Antarctic winter from three model cases: Base, NoCalbuco, and Noemission. We compare them with three lines from Solomon et al. (2016): TOMS/OMI observation, Solomon's simulation with, and without volcanic eruptions. The blue shade indicates the uncertainty of model simulations due to the horizontal resolution. The lower boundary of the blue shades assumes that only half of the most equatorward grid cell is within the 220 DU contour in the Base case. (b) The ozone hole differences between the cases with and without volcanic eruptions. The red line is from our model simulation, and the green line is from Solomon's simulation (Ivy et al., 2017). TOMS/OMI = Total Ozone Mapping Spectrometer/Ozone Monitoring Instrument.

Solomon et al. (2016). They state the ozone hole is 4.4 million km^2 larger due to volcanic eruptions. Figure 14b shows the trend of ozone hole area differences from our model and Solomon's simulations (Ivy et al., 2017). The two models show similar results on the effect of the volcanic eruptions on the ozone hole area. The largest difference between the modeled Base and Noemission cases is 6.7 million km^2 on 16 September 2015. The NoCalbuco case shows the *aged* volcanic sulfate aerosol contributes to half of the expansion of

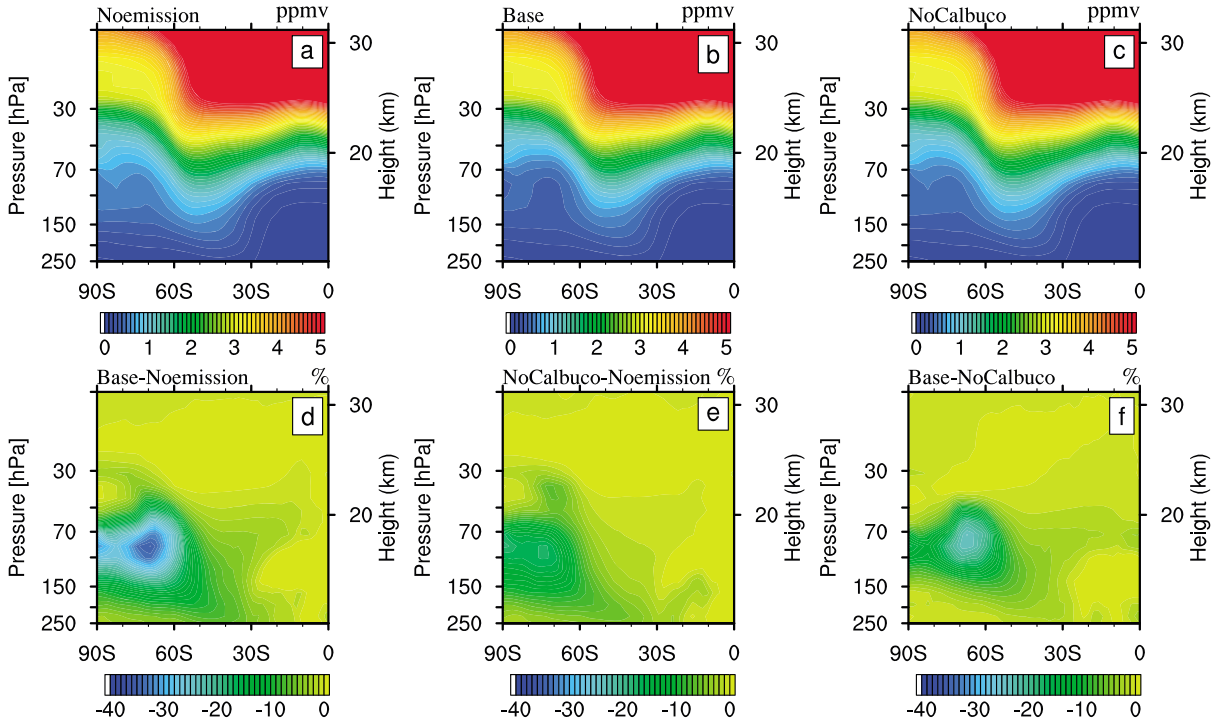

Figure 15. The zonal average ozone volume mixing ratio and the percentage differences between Base case, NoCalbuco case, and Noemission case from 15 to 30 September 2015.

the ozone hole. However, the numerical model has 2° grid cells, which must lead to an overestimate of the area of the ozone hole since the 220 DU contour will likely cover only part of the grid cell. If we assume that only half of the most equatorward grid cell is within the 220 DU contour, then the ozone hole area declines by ~ 1.5 million km^2 for the Base case after mid-September (shown as the lower boundary of the light blue area in Figure 14), which then places the Base case into best agreement with the TOMS/OMI data.

Figure 15 shows the zonal average ozone mass mixing ratio as well as the differences between the Base, NoCalbuco, and Noemission cases averaged over 15–30 September when the ozone hole starts to expand very quickly. The largest differences between the base case and the Noemission case (Figure 15c) are around 100 hPa and 70°S, which means the volcanic sulfate aerosol has the most effect on ozone depletion in this area. This result is consistent with the location of the volcanic sulfuric acid aerosol layers around 16 km shown in CALIPSO and modeled backscatter figures (Figures 3–6). This result is also consistent with Stone et al. (2017), who found the volcanic aerosol enhances the ozone depletion particularly at 150–100 hPa and 55–68°S. Sunlight first causes ozone depletion near the edge of the vortex. The peak change in ozone mixing ratio is over 35%, which is consistent with Solomon et al. (2016) who find the volcanic sulfate aerosol causes 40% more ozone depletion than if there had been no eruption. The NoCalbuco case, on the other hand, shows that the volcanic sulfate aerosols from eruptions previous to the Mount Calbuco have the most effect on ozone depletion from the South Pole to about 65°S around 100 hPa (Figure 15e). The percentage difference between the NoCalbuco and Noemission case is about 12%. The difference between the Base case and the NoCalbuco case indicates that the Mount Calbuco eruption has the strongest effect on the ozone depletion around 70°S and creates ~ 25% more ozone depletion.

5. Conclusion and Discussion

We investigate the impact of the 2015 Mount Calbuco eruption as well as the previous volcanic eruptions since 2011 on stratospheric aerosols, PSCs, and ozone chemistry in the SH. We compare the modeled size distributions, phase function, and Ångström exponent of NH and SH sulfuric acid aerosols after the Mount Calbuco eruption with the ones used in OMPS and OSIRIS satellites extinction retrievals, as well as the LOAC balloon observation. We compare the modeled optical properties of stratospheric sulfate aerosol and PSCs with the observations from CALIPSO, OMPS, and OSIRIS satellites. We also compare the gas phase HNO_3 and O_3 with MLS satellite observations. These comparisons help us to answer the four questions listed in section 1.

To answer question 1: The modeled size distribution in the NH and the two lognormal size distributions (L17 and B12) used by OMPS and OSIRIS extinction retrieval are similar to each other (Figure 1). In the SH, the WACCM/CARMA modeled size distribution and the two lognormal size distributions (L17 and B12) fit the LOAC observation at Reunion site mostly within the data error bars from 0.1 to 1 μm. The volcanic eruption significantly increased the number density, the volume density, and the extinction of the sulfuric acid aerosol in the SH compared with the NH. The modeled size distribution shows numerous small particles ($<$0.02 μm) mainly because of the nucleation of volcanic sulfuric acid aerosol. The WACCM/CARMA modeled volcanic sulfate aerosol reduces the aerosol Ångström exponent from 1.94 to 1.19 for the times and places of Table 3. The effective radii between the L17, B12, and modeled NH and SH size distributions are similar: 0.14 μm for L17 and B12; 0.16 for NH and 0.22 for SH. However, the phase function calculated from these size distributions shows inconsistency at backscatter SSA. For example, the phase function of L17 is about 2 times larger than the modeled NH and SH ones around 110° SSA. Two reasons can contribute to the inconsistency: the phase function varies significantly at backscatter SSA within stratospheric aerosol size ranges (shown in Figure 2a); the optical effective radii, which add weight on relatively large particle, show bigger differences between each size distribution than the effective radii. We conclude that the large variety of phase functions within stratospheric aerosol size ranges and the determination of the number density of relatively large stratospheric particles contribute to difficulties for satellites to retrieve the extinction.

To answer question 2: The backscatter coefficient observed by CALIPSO and calculated from the model shows that the volcanic sulfate aerosol is transported from midlatitude toward the South Pole (Figure 3). The sulfate aerosols are carried downward by mean motions and sedimentation as they move poleward. The modeled number density of the sulfate indicates the sulfate aerosol penetrates into the vortex in May and thereafter (Figures 4 and 5) due to the distortion of the vortex caused by planetary waves. The

backscatter value from CALIPSO (Figure 8) and the extinction value from OSIRIS (Figure 9) outside the Antarctic polar vortex are between the values from the Base case and the HalfSO2 case, which indicates that the SO_2 emission into the stratosphere is probably between 0.4 and 0.2 Tg. However, the OMPS extinction is below both model cases (Figure 9). The modeled PSCs and sulfate inside the vortex are smaller than the CALIPSO observation from June to September. Adding gravity waves increases the backscatter near the edge of the vortex, but not near the South Pole. Strong denitrification from PSCs in May limits the sulfate aerosol and PSC formation near the South Pole at later times.

To answer question 3: The simulated HNO_3 compared with MLS observations reveals a denitrification problem with the model (Figures 10). The model denitrified too early at 82°S and too much after July at 63°S. We ran a test case without STS to NAT nucleation because the large NAT particles that are responsible for most of the denitrification are formed from STS in our model (Figure 10). This test case helps to improve the denitrification but cannot explain the high depolarization and low backscatter areas observed by CALIPSO in late May (Figure 11). CALIPSO observations in Figures 11a and 11d indicate that large or medium sized NAT particles exist in late May, which is more consistent with the Base case results (Figures 11c and 11f). This conclusion is also supported by previous studies (Lambert et al., 2012; Zhu, Toon, Lambert, et al., 2017). Either an increased homogeneous nucleation rate or heterogeneous nucleation of NAT on STS may be needed to nucleate NAT that does not denitrify too quickly and shows a large depolarization in late May. The source of these nuclei could be the micrometeoroids as suggested by Hoyle et al. (2013).

To answer question 4: The volcanic sulfate aerosol from the Mount Calbuco eruption and previous eruptions since 2011 enhances ozone depletion in September and October. The O_3 in the Base case is depleted more than 35% (Figure 15c), and the ozone hole size is 4.8 million km^2 larger (Figure 14) than in the Noemission case in September. This result is generally consistent with Solomon et al. (2016). The Base case shows that the start date of the ozone hole is 3 days later than the TOMS/OMI observation. The peak ozone hole area in the NoCalbuco case is closest to TOMS/OMI among our three model simulations. However, the area calculation is impacted by the spatial resolution of the model, so the error bar of the Base case area overlaps the TOMS/OMI data. The difference of O_3 between the Base case and the NoCalbuco case indicates that the Mount Calbuco eruption depletes ~ 25% of O_3 (Figure 15f) near 70°S and creates an additional 2.4 million km^2 of ozone hole area in September in our simulation (Figure 14). The largest difference in O_3 due to the Mount Calbuco volcanic injection is found around 100 hPa and 70°S (Figure 15f). This location is consistent with the volcanic sulfate layers observed at 16 km and with the conclusions from Stone et al. (2017) who found the ozone depletion was enhanced at 55–68°S and between 100 and 150 hPa. The previous eruptions increase the SAD near the South Pole compared with the case without any eruptions. And the Mount Calbuco eruption increases the SAD from the Pole toward midlatitude. Both Solomon et al. (2016) and our model show that the SAD from sulfate aerosol and STS in the case with volcanic eruptions is twice as large as in the case without any volcanic eruptions and covers a much larger geographic area from the South Pole to ~ 20°S.

Acknowledgments
The work at the University of Colorado was supported by NASA grant NNX16AQ37G and National Science Foundation (NSF) grant PLR1643701. V. Lynn Harvey acknowledges support from NSF CEDAR grant 1343031, NASA LWS grant NNX14AH54G, and NASA HGI grant NNX17AB80G. We thank Anja Schmidt for her help with the volcanic emission database. We thank Susan Solomon for providing the data used in Solomon et al. (2016). We thank Alyn Lambert for his help with the MLS data. The authors thank the LPC2E and UMS balloon launching team for their technical collaboration. LOAC measurements have been supported by WP7 of the VOLTAIRE LabEx (VOLatils—Terre, Atmosphère et Interactions-Ressources et Environnement), convention number ANR–10–LABX–100–01. WACCM is a component of NCAR's CESM, which is supported by NSF and the Office of Science of the U.S. Department of Energy. We would like to acknowledge high-performance computing support from Cheyenne (doi:10.5065/D6RX99HX) provided by NCAR's Computational and Information Systems Laboratory (CISL), sponsored by the NSF. The source code for the WACCM/CARMA model used in this study is freely available at http://www2.cesm.ucar.edu/ upon registration. The developing version of this model, as well as the data, and input files necessary to reproduce the experiments are available from the authors upon request (yunqian.zhu@colorado.edu). The model data are archived at the Toon Aerosol Research Group computers. The data that form or illustrate the key results or images for this paper are available at Zhu, Y. (21 August 2018), Calbuco WACCM/CARMA simulation, retrieved from osf.io/rmqyt. The CALIPSO date are available at the NASA Langley Atmospheric Science Data Center (ASDC) (http://eosweb.larc.nasa.gov/). The OMPS data are available at Ozone and Air Quality website (https://ozoneaq.gsfc.nasa.gov/). The MLS data are available at http://mls.jpl.nasa.gov/. The OSIRIS data are available at http://odin-osiris.usask.ca/.

References

Bardeen, C. G., Toon, O. B., Jensen, E. J., Hervig, M. E., Randall, C. E., Benze, S., et al. (2010). Numerical simulations of the three-dimensional distribution of polar mesospheric clouds and comparisons with Cloud Imaging and Particle Size (CIPS) experiment and the Solar Occultation for Ice Experiment (SOFIE) observations. *Journal of Geophysical Research*, *115*, D10204. https://doi.org/10.1029/2009JD012451

Bardeen, C. G., Toon, O. B., Jensen, E. J., Marsh, D. R., & Harvey, V. L. (2008). Numerical simulations of the three-dimensional distribution of meteoric dust in the mesosphere and upper stratosphere. *Journal of Geophysical Research*, *113*, D17202. https://doi.org/10.1029/2007JD009515

Bègue, N., Vignelles, D., Berthet, G., Portafaix, T., Payen, G., Jégou, F., et al. (2017). Long-range transport of stratospheric aerosols in the Southern Hemisphere following the 2015 Calbuco eruption. *Atmospheric Chemistry and Physics*, *17*(24), 15,019–15,036. https://doi.org/10.5194/acp-17-15019-2017

Bourassa, A. E., Rieger, L. A., Lloyd, N. D., & Degenstein, D. A. (2012). Odin-OSIRIS stratospheric aerosol data product and SAGE III intercomparison. *Atmospheric Chemistry and Physics*, *12*(1), 605–614. https://doi.org/10.5194/acp-12-605-2012

Campbell, P., Mills, M., & Deshler, T. (2014). The global extent of the mid stratospheric CN layer: A three-dimensional modeling study. *Journal of Geophysical Research: Atmospheres*, *119*, 1015–1030. https://doi.org/10.1002/2013JD020503

Crutzen, P. J. (1976). The possible importance of CSO for the sulfate layer of the stratosphere. *Geophysical Research Letters*, *3*(2), 73–76. https://doi.org/10.1029/GL003i002p00073

Deshler, T., Hervig, M. E., Hofmann, D. J., Rosen, J. M., & Liley, J. B. (2003). Thirty years of in situ stratospheric aerosol size distribution measurements from Laramie, Wyoming (41°N), using balloon-borne instruments. *Journal of Geophysical Research*, *108*(D5), 4167. https://doi.org/10.1029/2002JD002514

Diallo, M., Ploeger, F., Konopka, P., Birner, T., Müller, R., Riese, M., et al. (2017). Significant contributions of volcanic aerosols to decadal changes in the stratospheric circulation. *Geophysical Research Letters*, *44*, 10,780–10,791. https://doi.org/10.1002/2017GL074662

Dunkerton, T. J., & Delisi, D. P. (1986). Evolution of potential vorticity in the winter stratosphere of January-February 1979. *Journal of Geophysical Research*, *91*(D1), 1199–1208. https://doi.org/10.1029/JD091iD01p01199

Dye, J. E., Baumgardner, D., Gandrud, B. W., Kawa, S. R., Kelly, K. K., Loewenstein, M., et al. (1992). Particle size distributions in arctic polar stratospheric clouds, growth and freezing of sulfuric acid droplets, and implications for cloud formation. *Journal of Geophysical Research*, *97*(D8), 8015–8034. https://doi.org/10.1029/91JD02740

English, J. M., Toon, O. B., & Mills, M. J. (2013). Microphysical simulations of large volcanic eruptions: Pinatubo and Toba. *Journal of Geophysical Research: Atmospheres*, *118*, 1880–1895. https://doi.org/10.1002/jgrd.50196

English, J. M., Toon, O. B., Mills, M. J., & Yu, F. (2011). Microphysical simulations of new particle formation in the upper troposphere and lower stratosphere. *Atmospheric Chemistry and Physics*, *11*(17), 9303–9322. https://doi.org/10.5194/acp-11-9303-2011

Flynn, L. E., Seftor, C. J., Larsen, J. C., & Xu, P. (2006). The ozone mapping and profiler suite. In *Earth science satellite remote sensing* (pp. 279–296). Berlin, Heidelberg: Springer.

Garcia, R. R., Marsh, D. R., Kinnison, D. E., Boville, B. A., & Sassi, F. (2007). Simulation of secular trends in the middle atmosphere, 1950–2003. *Journal of Geophysical Research*, *112*, D09301. https://doi.org/10.1029/2006JD007485

Harvey, V. L., Pierce, R. B., Fairlie, T. D., & Hitchman, M. H. (2002). A climatology of stratospheric polar vortices and anticyclones. *Journal of Geophysical Research*, *107*(D20), 4442. https://doi.org/10.1029/2001JD001471

Hofmann, D., Barnes, J., O'Neill, M., Trudeau, M., & Neely, R. (2009). Increase in background stratospheric aerosol observed with lidar at Mauna Loa Observatory and Boulder, Colorado. *Geophysical Research Letters*, *36*, L15808. https://doi.org/10.1029/2009GL039008

Hofmann, D. J., & Oltmans, S. J. (1993). Anomalous Antarctic ozone during 1992: Evidence for Pinatubo volcanic aerosol effects. *Journal of Geophysical Research*, *98*(D10), 18,555–18,561. https://doi.org/10.1029/93JD02092

Hoyle, C. R., Engel, I., Luo, B. P., Pitts, M. C., Poole, L. R., Grooß, J.-U., & Peter, T. (2013). Heterogeneous formation of polar stratospheric clouds—Part 1: Nucleation of nitric acid trihydrate (NAT). *Atmospheric Chemistry and Physics*, *13*(18), 9577–9595. https://doi.org/10.5194/acp-13-9577-2013

Ivy, D. J., Solomon, S., Kinnison, D., Mills, M. J., Schmidt, A., & Neely, R. R. (2017). The influence of the Calbuco eruption on the 2015 Antarctic ozone hole in a fully coupled chemistry-climate model. *Geophysical Research Letters*, *44*, 2556–2561. https://doi.org/10.1002/2016GL071925

Kinnison, D. E., Brasseur, G. P., Walters, S., Garcia, R. R., Marsh, D. R., Sassi, F., et al. (2007). Sensitivity of chemical tracers to meteorological parameters in the MOZART-3 chemical transport model. *Journal of Geophysical Research*, *112*, D20302. https://doi.org/10.1029/2006JD007879

Koop, T., Luo, B., Tsias, A., & Peter, T. (2000). Water activity as the determinant for homogeneous ice nucleation in aqueous solutions. *Nature*, *406*(6796), 611–614. https://doi.org/10.1038/35020537

Kovilakam, M., & Deshler, T. (2015). On the accuracy of stratospheric aerosol extinction derived from in situ size distribution measurements and surface area density derived from remote SAGE II and HALOE extinction measurements. *Journal of Geophysical Research: Atmospheres*, *120*, 8426–8447. https://doi.org/10.1002/2015JD023303

Kunz, A., Pan, L. L., Konopka, P., Kinnison, D. E., & Tilmes, S. (2011). Chemical and dynamical discontinuity at the extratropical tropopause based on START08 and WACCM analyses. *Journal of Geophysical Research*, *116*, D24302. https://doi.org/10.1029/2011JD016686

Lamarque, J.-F., Emmons, L. K., Hess, P. G., Kinnison, D. E., Tilmes, S., Vitt, F., et al. (2012). CAM-Chem: Description and evaluation of interactive atmospheric chemistry in the Community Earth System Model. *Geoscientific Model Development*, *5*(2), 369–411. https://doi.org/10.5194/gmd-5-369-2012

Lambert, A., Santee, M. L., Wu, D. L., & Chae, J. H. (2012). A-train CALIOP and MLS observations of early winter Antarctic polar stratospheric clouds and nitric acid in 2008. *Atmospheric Chemistry and Physics*, *12*(6), 2899–2931. https://doi.org/10.5194/acp-12-2899-2012

Livesey, N. J. (2015). Earth Observing System (EOS) Aura Microwave Limb Sounder (MLS) version 4.2 x Level 2 Data Quality and Description Document, 91109–8099, version 4.2 x, *Jet Propuls. Lab., Calif. Insti. Tech., Pasadena, Calif*.

Llewellyn, E. J., Lloyd, N. D., Degenstein, D. A., Gattinger, R. L., Petelina, S. V., Bourassa, A. E., et al. (2004). The OSIRIS instrument on the Odin spacecraft. *Canadian Journal of Physics*, *82*(6), 411–422. https://doi.org/10.1139/p04-005

Loughman, R., Bhartia, P. K., Chen, Z., Xu, P., Nyaku, E., & Taha, G. (2017). The Ozone Mapping and Profiler Suite (OMPS) Limb Profiler (LP) version 1 aerosol extinction retrieval algorithm: Theoretical basis. *Atmospheric Measurement Techniques Discussions*, *2017*, 1–34. https://doi.org/10.5194/amt-2017-299

Lurton, T., Jégou, F., Berthet, G., Renard, J.-B., Clarisse, L., Schmidt, A., et al. (2018). Model simulations of the chemical and aerosol microphysical evolution of the Sarychev Peak 2009 eruption cloud compared to in situ and satellite observations. *Atmospheric Chemistry and Physics*, *18*(5), 3223–3247. https://doi.org/10.5194/acp-18-3223-2018

Lurton, T., Renard, J.-B., Vignelles, D., Jeannot, M., Akiki, R., Mineau, J.-L., & Tonnelier, T. (2014). Light scattering at small angles by atmospheric irregular particles: Modelling and laboratory measurements. *Atmospheric Measurement Techniques*, *7*(4), 931–939. https://doi.org/10.5194/amt-7-931-2014

Manney, G. L., Zurek, R. W., O'Neill, A., & Swinbank, R. (1994). On the motion of air through the stratospheric polar vortex. *Journal of the Atmospheric Sciences*, *51*(20), 2973–2994. https://doi.org/10.1175/1520-0469(1994)051<2973:OTMOAT>2.0.CO;2

Marsh, D. R., Mills, M. J., Kinnison, D. E., Lamarque, J.-F., Calvo, N., & Polvani, L. M. (2013). Climate change from 1850 to 2005 simulated in CESM1(WACCM). *Journal of Climate*, *26*(19), 7372–7391. https://doi.org/10.1175/JCLI-D-12-00558.1

Mills, M. J., Schmidt, A., Easter, R., Solomon, S., Kinnison, D. E., Ghan, S. J., et al. (2016). Global volcanic aerosol properties derived from emissions, 1990–2014, using CESM1(WACCM). *Journal of Geophysical Research: Atmospheres*, *121*, 2332–2348. https://doi.org/10.1002/2015JD024290

Mills, M. J., Toon, O. B., Turco, R. P., Kinnison, D. E., & Garcia, R. R. (2008). Massive global ozone loss predicted following regional nuclear conflict. *Proceedings of the National Academy of Sciences of the United States of America*, *105*(14), 5307–5312.

Mills, M. J., Toon, O. B., Vaida, V., Hintze, P. E., Kjaergaard, H. G., Schofield, D. P., & Robinson, T. W. (2005). Photolysis of sulfuric acid vapor by visible light as a source of the polar stratospheric CN layer. *Journal of Geophysical Research*, *110*, D08201. https://doi.org/10.1029/2004JD005519

Mishchenko, M. I., & Travis, L. D. (1998). Capabilities and limitations of a current FORTRAN implementation of the T-matrix method for randomly oriented, rotationally symmetric scatterers. *Journal of Quantitative Spectroscopy and Radiative Transfer*, *60*(3), 309–324. https://doi.org/10.1016/S0022-4073(98)00008-9

Neely, R. R., Toon, O. B., Solomon, S., Vernier, J.-P., Alvarez, C., English, J. M., et al. (2013). Recent anthropogenic increases in SO_2 from Asia have minimal impact on stratospheric aerosol. *Geophysical Research Letters*, *40*, 999–1004. https://doi.org/10.1002/grl.50263

Pitts, M. C., Poole, L. R., & Thomason, L. W. (2009). CALIPSO polar stratospheric cloud observations: Second-generation detection algorithm and composition discrimination. *Atmospheric Chemistry and Physics*, *9*(19), 7577–7589. https://doi.org/10.5194/acp-9-7577-2009

Pruppacher, H. R., & Klett, J. D. (1997). *Microphysics of clouds and precipitation* (2nd ed.). Dordrecht, Boston: Kluwer Academic Publishers.
Pueschel, R. F., Russell, P. B., Allen, D. A., Ferry, G. V., Snetsinger, K. G., Livingston, J. M., & Verma, S. (1994). Physical and optical properties of the Pinatubo volcanic aerosol: Aircraft observations with impactors and a Sun-tracking photometer. *Journal of Geophysical Research*, *99*(D6), 12,915–12,922. https://doi.org/10.1029/94JD00621
Renard, J.-B., Dulac, F., Berthet, G., Lurton, T., Vignelles, D., Jégou, F., et al. (2016a). LOAC: A small aerosol optical counter/sizer for ground-based and balloon measurements of the size distribution and nature of atmospheric particles—Part 1: Principle of measurements and instrument evaluation. *Atmospheric Measurement Techniques*, *9*(4), 1721–1742. https://doi.org/10.5194/amt-9-1721-2016
Renard, J.-B., Dulac, F., Berthet, G., Lurton, T., Vignelles, D., Jégou, F., et al. (2016b). LOAC: A small aerosol optical counter/sizer for ground-based and balloon measurements of the size distribution and nature of atmospheric particles—Part 2: First results from balloon and unmanned aerial vehicle flights. *Atmospheric Measurement Techniques*, *9*(8), 3673–3686. https://doi.org/10.5194/amt-9-3673-2016
Ridley, D. A., Solomon, S., Barnes, J. E., Burlakov, V. D., Deshler, T., Dolgii, S. I., et al. (2014). Total volcanic stratospheric aerosol optical depths and implications for global climate change. *Geophysical Research Letters*, *41*, 7763–7769. https://doi.org/10.1002/2014GL061541
Rienecker, M. M., Suarez, M. J., Gelaro, R., Todling, R., Bacmeister, J., Liu, E., et al. (2011). MERRA: NASA's Modern-Era Retrospective Analysis for Research and Applications. *Journal of Climate*, *24*(14), 3624–3648. https://doi.org/10.1175/JCLI-D-11-00015.1
Santer, B. D., Bonfils, C., Painter, J. F., Zelinka, M. D., Mears, C., Solomon, S., et al. (2014). Volcanic contribution to decadal changes in tropospheric temperature. *Nature Geoscience*, *7*, 185–189.
Schoeberl, M. R. (2007). The EOS Aura mission. In *Observing systems for atmospheric composition* (pp. 64–70). New York: Springer.
Solomon, S., Daniel, J. S., Neely, R. R., Vernier, J.-P., Dutton, E. G., & Thomason, L. W. (2011). The persistently variable "background" stratospheric aerosol layer and global climate change. *Science*, *333*(6044), 866–870.
Solomon, S., Ivy, D. J., Kinnison, D., Mills, M. J., Neely, R. R., & Schmidt, A. (2016). Emergence of healing in the Antarctic ozone layer. *Science*, *353*(6296), 269–274.
Solomon, S., Kinnison, D., Bandoro, J., & Garcia, R. (2015). Simulation of polar ozone depletion: An update. *Journal of Geophysical Research: Atmospheres*, *120*, 7958–7974. https://doi.org/10.1002/2015JD023365
Solomon, S., Portmann, R. W., Garcia, R. R., Thomason, L. W., Poole, L. R., & McCormick, M. P. (1996). The role of aerosol variations in anthropogenic ozone depletion at northern midlatitudes. *Journal of Geophysical Research*, *101*(D3), 6713–6727. https://doi.org/10.1029/95JD03353
Solomon, S., Portmann, R. W., Sasaki, T., Hofmann, D. J., & Thompson, D. W. J. (2005). Four decades of ozonesonde measurements over Antarctica. *Journal of Geophysical Research*, *110*, D21311. https://doi.org/10.1029/2005JD005917
SPARC (2006). SPARC Assessment of Stratospheric Aerosol Properties (ASAP), Edited by L. Thomason and T. Peter, SPARC Office.
Stone, K. A., Solomon, S., Kinnison, D. E., Pitts, M. C., Poole, L. R., Mills, M. J., et al. (2017). Observing the impact of Calbuco volcanic aerosols on south polar ozone depletion in 2015. *Journal of Geophysical Research: Atmospheres*, *122*, 11,862–11,879. https://doi.org/10.1002/2017JD026987
Tabazadeh, A., Djikaev, Y. S., Hamill, P., & Reiss, H. (2002). Laboratory evidence for surface nucleation of solid polar stratospheric cloud particles. *The Journal of Physical Chemistry. A*, *106*(43), 10,238–10,246. https://doi.org/10.1021/jp021045k
Tie, X., & Brasseur, G. (1995). The response of stratospheric ozone to volcanic eruptions: Sensitivity to atmospheric chlorine loading. *Geophysical Research Letters*, *22*(22), 3035–3038. https://doi.org/10.1029/95GL03057
Tie, X., Brassuer, G. P., Granier, C., De Rudder, A., & Larsen, N. (1996). Model study of polar stratospheric clouds and their effect on stratospheric ozone: 2. Model results. *Journal of Geophysical Research*, *101*(D7), 12,575–12,584. https://doi.org/10.1029/96JD00403
Toon, O. B., Hamill, P., Turco, R. P., & Pinto, J. (1986). Condensation of HNO_3 and HCl in the winter polar stratospheres. *Geophysical Research Letters*, *13*(12), 1284–1287. https://doi.org/10.1029/GL013i012p01284
Toon, O. B., Turco, R. P., Jordan, J., Goodman, J., & Ferry, G. (1989). Physical processes in polar stratospheric ice clouds. *Journal of Geophysical Research*, *94*(D9), 11,359–11,380. https://doi.org/10.1029/JD094iD09p11359
Trickl, T., Giehl, H., Jäger, H., & Vogelmann, H. (2013). 35 yr of stratospheric aerosol measurements at Garmisch-Partenkirchen: From Fuego to Eyjafjallajökull, and beyond. *Atmospheric Chemistry and Physics*, *13*(10), 5205–5225. https://doi.org/10.5194/acp-13-5205-2013
Vernier, J.-P., Thomason, L. W., Pommereau, J.-P., Bourassa, A., Pelon, J., Garnier, A., et al. (2011). Major influence of tropical volcanic eruptions on the stratospheric aerosol layer during the last decade. *Geophysical Research Letters*, *38*, L12807. https://doi.org/10.1029/2011GL047563
Wegner, T., Grooß, J.-U., von Hobe, M., Stroh, F., Sumińska-Ebersoldt, O., Volk, C. M., et al. (2012). Heterogeneous chlorine activation on stratospheric aerosols and clouds in the Arctic polar vortex. *Atmospheric Chemistry and Physics*, *12*(22), 11,095–11,106. https://doi.org/10.5194/acp-12-11095-2012
Winker, D. M., Hunt, W. H., & McGill, M. J. (2007). Initial performance assessment of CALIOP. *Geophysical Research Letters*, *34*, L19803. https://doi.org/10.1029/2007GL030135
Zhu, Y., Toon, O. B., Lambert, A., Kinnison, D. E., Bardeen, C., & Pitts, M. C. (2017). Development of a polar stratospheric cloud model within the Community Earth System Model: Assessment of 2010 Antarctic winter. *Journal of Geophysical Research: Atmospheres*, *122*, 10,418–10,438. https://doi.org/10.1002/2017JD027003
Zhu, Y., Toon, O. B., Lambert, A., Kinnison, D. E., Brakebusch, M., Bardeen, C. G., et al. (2015). Development of a polar stratospheric cloud model within the Community Earth System Model using constraints on type I PSCs from the 2010–2011 Arctic winter. *Journal of Advances in Modeling Earth Systems*, *7*, 551–585. https://doi.org/10.1002/2015MS000427
Zhu, Y., Toon, O. B., Pitts, M. C., Lambert, A., Bardeen, C., & Kinnison, D. E. (2017). Comparing simulated PSC optical properties with CALIPSO observations during the 2010 Antarctic winter. *Journal of Geophysical Research: Atmospheres*, *122*, 1175–1202. https://doi.org/10.1002/2016JD025191